Energy dissipation in two-dimensional unsteady plunging breakers and an eddy viscosity model

ZHIGANG TIAN[1], MARC PERLIN[1]†
AND WOOYOUNG CHOI[2]

[1]Naval Architecture and Marine Engineering, University of Michigan, Ann Arbor, MI 48109, USA

[2]Department of Mathematical Sciences, New Jersey Institute of Technology, Newark, NJ 07102, USA

An experimental study of energy dissipation in two-dimensional unsteady plunging breakers and an eddy viscosity model to simulate the dissipation due to wave breaking are reported in this paper. Measured wave surface elevations are used to examine the characteristic time and length scales associated with wave groups and local breaking waves, and to estimate and parameterize the energy dissipation and dissipation rate due to wave breaking. Numerical tests using the eddy viscosity model are performed and we find that the numerical results well capture the measured energy loss. In our experiments, three sets of characteristic time and length scales are defined and obtained: global scales associated with the wave groups, local scales immediately prior to breaking onset and post-breaking scales. Correlations among these time and length scales are demonstrated. In addition, for our wave groups, wave breaking onset predictions using the global and local wave steepnesses are found based on experimental results. Breaking time and breaking horizontal length scales are determined with high-speed imaging, and are found to depend approximately linearly on the local wave steepness. The two scales are then used to determine the energy dissipation rate, which is the ratio of the energy loss to the breaking time scale. Our experimental results show that the local wave steepness is highly correlated with the measured dissipation rate, indicating that the local wave steepness may serve as a good wave-breaking-strength indicator. To simulate the energy dissipation due to wave breaking, a simple eddy viscosity model is proposed and validated with our experimental measurements. Under the small viscosity assumption, the leading-order viscous effect is incorporated into the free-surface boundary conditions. Then, the kinematic viscosity is replaced with an eddy viscosity to account for energy loss. The breaking time and length scales, which depend weakly on wave breaking strength, are applied to evaluate the magnitude of the eddy viscosity using dimensional analysis. The estimated eddy viscosity is of the order of 10^{-3} m^2 s^{-1} and demonstrates a strong dependence on wave breaking strength. Numerical simulations with the eddy viscosity estimation are performed to compare to the experimental results. Good agreement as regards energy dissipation due to wave breaking and surface profiles after wave breaking is achieved, which illustrates that the simple eddy viscosity model functions effectively.

† Email address for correspondence: perlin@umich.edu

1. Introduction

Wave breaking has been of interest since the very beginning of the scientific study of water waves. Due to its significant role in air–sea interaction and its important effects on upper ocean dynamics and possibly climate change, wave breaking has received more and more attention recently. The laboratory study by Rapp & Melville (1990) provided remarkable insight on wave breaking. Banner & Peregrine (1993) presented a comprehensive review of both field measurements and laboratory studies of breaking waves, and wave-breaking-associated secondary effects were discussed in their study. Later, Melville (1996) focused on the role of surface-wave breaking in air–sea interaction and presented a thorough discussion on wave breaking dynamics. More recently, Perlin & Schultz (2000) reviewed capillary effects on surface waves and discussed breaking onset and breaking models of forced standing waves. Duncan (2001) provided experimental measurements of the surface profiles of spilling breakers and revealed important kinematics associated with them.

Although extensive research on breaking waves has been reported, the kinematics and dynamics of breaking waves remain an open question. For example, a robust wave breaking criterion remains an enigma; measuring the velocity field during active wave breaking continues to be a formidable challenge, and robust and reliable methods to characterize, quantify and simulate the energy dissipation due to wave breaking have not been developed yet.

As regards wave breaking criteria, the limiting wave steepness, $ka \approx 0.44$, has been used to indicate wave breaking onset since the study by Stokes (1880). However, this criterion is sensitive to three-dimensional effects (Nepf, Wu & Chan 1998) and wave directionality (Wu & Nepf 2002). A second type of wave criterion is based on local wave kinematics and states that wave breaking occurs when the horizontal crest particle velocity exceeds the linear wave phase speed. Particle image velocimetry (PIV) measurements by Perlin, He & Bernal (1996) and Chang & Liu (1998) support this criterion; however, Stansell & MacFarlane's (2002) study demonstrates that wave breaking can occur even when the horizontal crest particle velocity is less than the phase speed. Recently, wave breaking criteria based on local wave energy provided promising results (Schultz, Huh & Griffin 1994; Banner & Tian 1998). Particularly, the numerical study by Song & Banner (2002) presents a dimensionless growth rate, $\delta(t)$, based on the local wave energy density and the local wavenumber to predict the onset of wave breaking. A threshold for $\delta(t)$ of $(1.4 \pm 0.1) \times 10^{-3}$ is proposed to distinguish wave groups that lead to breaking from those that do not. Banner & Peirson (2007) experimentally reproduced the numerical tests by Song and Banner and provided an experimental validation of the criterion. Tian, Perlin & Choi (2008) performed experimental measurements of wave groups with different group structure from that of Song and Banner. They found that the criterion is sensitive to the choice of local wavenumber, but that a particular wavenumber based on local wave geometry differentiates wave groups that lead to breaking from those that do not.

Measurement of surface profiles and velocity fields associated with wave breaking is very important in understanding wave breaking kinematics and in providing validation of numerical simulations of breaking waves (Longuet-Higgins & Cokelet 1976; Dommermuth et al. 1988; Skyner 1996; Grue et al. 2003; Grue & Jensen 2006). Duncan et al. (1999) managed to capture breaking crest profile histories of gentle spillers with high-speed imaging using a thin laser sheet. The profile histories suggest that the wave breaking process begins with a bulbous formation at the front-face toe of the breaking crest. Further development of the bulge (a moving pressure disturbance)

generates capillary waves. Similar parasitic capillary waves were observed previously on the lower front face of plunging breakers by Perlin *et al.* (1996), who conducted a detailed experimental study on deep-water plungers. Their PIV measurements show that the velocity fields under the breaking crests decay rapidly with depth and that they are essentially irrotational until incipient breaking occurs. Chang & Liu (1998) did similar experiments, but focused on velocity, acceleration and vorticity measurements. They reported that the overturning jet has a horizontal velocity 68 % greater than the linear phase speed and that its acceleration is as high as $1.1g$ as the jet collapses near perpendicularly to the horizontal water surface. Melville, Veron & White (2002) used digital PIV to measure the velocity field under breaking waves. Their measurements reveal that wave breaking produces at least one coherent vortex, which propagates slowly downstream and may suppress short waves. Their experimental study also confirms that 90 % of the total energy loss occurs within the first four wave periods, which is consistent with the study by Rapp & Melville (1990). Although these experiments provide valuable measurements of the velocity field prior to and/or after active wave breaking, they were unable to measure the velocity field beneath the breaking crest during active breaking, as the PIV technique is rendered ineffective due to the opacity of the two-phase flow and the laser sheet scattering by the entrained bubbles and the free surface.

Estimation of the energy dissipation rate due to wave breaking remains another challenging problem. The most reliable method to estimate the energy dissipation rate requires direct measurement of the velocity field and the surface profile over a fairly large field of view throughout the breaking process, and it has proved impractical for both laboratory and field measurements. Alternatively, one may first estimate the energy loss due to wave breaking with surface elevation measurements and control volume analysis, and then evaluate the dissipation rate with proper breaking time scale. Lowen & Melville (1991) measured the duration of the acoustic sound generated by wave breaking; Melville (1994) applied their measurements to deduce the associated energy dissipation rate. Similarly, Drazen, Melville & Lenain (2008) estimated the energy loss due to plunging breakers and recorded the acoustic sound to infer the breaking time scale, based on which the energy loss rate was assessed. This method implicitly assumes that the dissipation rate is constant throughout the breaking process. However, wave breaking is unsteady (Melville 1994) and the dissipation rate may not remain constant. As demonstrated by Lamarre & Melville (1991), entraining air into water, which occurs within a small fraction of a wave period, expends 30–50 % of the energy dissipated; on the other hand, 90 % of the total energy loss is dissipated within the first four wave periods after wave breaking, and the remainder decays as t^{-1} (Rapp & Melville 1990; Melville *et al.* 2002). Nevertheless, a large amount of energy is dissipated rapidly over a short period so that a constant dissipation rate assumption may be a reasonable approximation.

Seminal work on characterizing the energy loss rate arose from the experimental work of Duncan (1981, 1983), who measured the drag per unit length due to quasi-steady breaking waves generated with a submerged hydrofoil. His measurements illustrated that the drag per unit width scales with the fourth power of the breaking crest speed: $F_b \sim u_{br}^4$, where u_{br} is the breaking wave crest velocity. Thus, the energy dissipation rate was determined to be $\varepsilon \sim u_{br}^5$ (Duncan 1981; Phillips 1985; Thorpe 1993; Melville 1994). Recently, Banner & Peirson (2007) rewrote the proportional relation as $\varepsilon = bc_b^5$, with c_b being the breaking wave phase speed and b a proportional parameter, which is related to wave breaking strength. They argued that the new

proportional relation is consistent with energy and momentum flux transfers while the original one is not.

The proportional parameter, b, in the above relation is usually considered as an indication of wave breaking strength, and hence, it is termed the wave breaking strength parameter (Banner & Peirson 2007; Drazen *et al.* 2008). Extensive laboratory experiments and field measurements have been conducted to quantify this constant (Duncan 1981, 1983; Phillips 1985; Thorpe 1993; Melville 1994; Phillips, Posner & Hansen 2001; Melville & Matusov 2002; Banner & Peirson 2007; Drazen *et al.* 2008; Gemmrich, Banner & Garret 2008). However, reported results span two orders of magnitude. In general, field measurements provide a much smaller estimation than laboratory experiments. This discrepancy remains unresolved (Gemmrich *et al.* 2008).

A second wave breaking strength parameter, δ_{br}, has been proposed recently by Song & Banner (2002), whose study suggests that the magnitude of the breaking criterion parameter, $\delta(t)$, just prior to wave breaking, indicates wave breaking strength. Banner & Peirson (2007) and Tian *et al.* (2008) performed experiments and demonstrated that δ_{br} increases as wave breaking intensifies. In addition, an approximately linear relationship between δ_{br} and b is shown in figure 8(*b*) of Banner & Peirson (2007).

Along with the difficulties of wave breaking onset prediction, energy dissipation rate estimation and wave breaking strength quantification, robust numerical studies of breaking waves in deep water are few. One of the first numerical studies of breaking waves was completed by Longuet-Higgins & Cokelet (1976) using the boundary integral method (BIM). Their computation was successful to wave-crest overturning, but, as expected, failed when the overturning jet collapsed on the water surface. The success of the volume of fluid method (VoF) provides an alternative way to simulate wave breaking. Chen *et al.* (1999) used the VoF method to simulate a two-dimensional plunging breaker. Their numerical study captured key kinematic characteristics of wave breaking, including the overturning motion, the gas entrainment and the surface splash-up phenomena. In addition, 80 % of the pre-breaking energy was dissipated within the first three wave periods following breaking. More recently, Sullivan, McWilliams & Melville (2004) developed a stochastic wave breaking model based on laboratory experiments and field measurements, and employed direct numerical simulation (DNS) to evaluate the model with an isolated breaking event to estimate wave breaking effects on the ocean surface boundary layer. With the breaker model, they reproduced some key dynamic features of a breaking event, such as the mean kinetic energy decay rate and the coherent vortex structure (Melville *et al.* 2002).

In this study, we have no intention of developing or using complicated numerical models of wave breaking to model the breaking process; rather, we apply a simple eddy viscosity model to simulate energy dissipation in two-dimensional unsteady plunging breakers. In addition, detailed experiments are performed to determine wave characteristics associated with wave groups and local breaking waves, further validate the wave breaking criterion of Song & Banner (2002), measure the time and length scales of active wave breaking, estimate the energy dissipation and dissipation rate due to breaking waves and quantify the wave breaking strength. The measured time and length scales associated with active wave breaking are used to determine the eddy viscosity using dimensional analysis and/or the turbulence energy dissipation rate analysis according to Melville (1994).

The remainder of the paper is organized as follows. Subsequent to the Introduction, we describe the experimental setup and surface profile measurements with wave probes and high-speed imaging. Detailed experimental results on breaking-wave time and length scale measurements, energy loss and energy loss rate estimation, and eddy
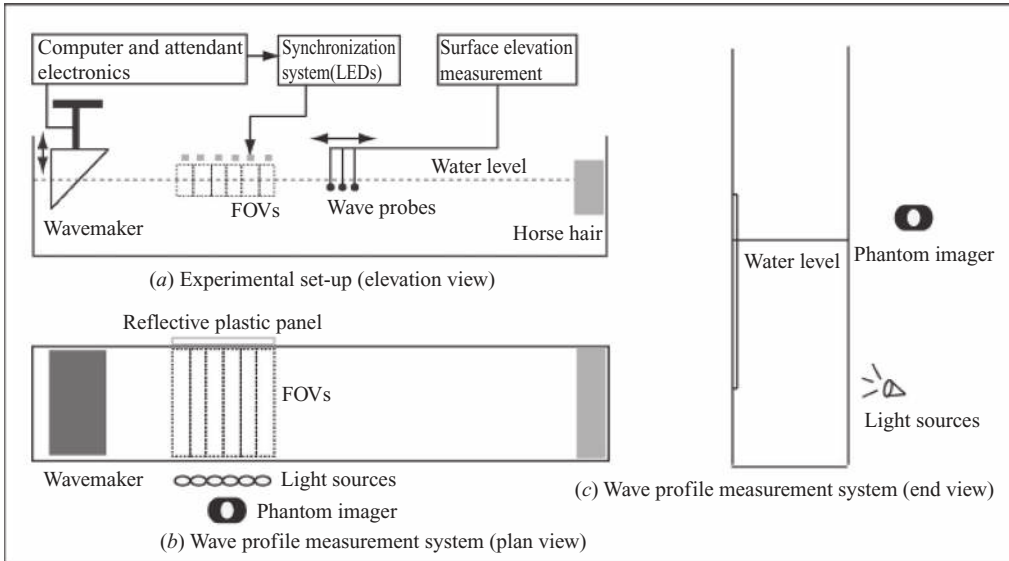
FIGURE 1. Sketch of the experimental setup for the surface elevation measurements. FOV indicates field of view. (Not to scale.)

viscosity assessment are provided in § 3. Section 4 presents an eddy viscosity model for weakly damped waves in which the small viscous effect is incorporated into the inviscid free-surface boundary conditions; in addition, numerical simulations using the eddy viscosity model to determine energy dissipation due to wave breaking are presented and compared with experimental measurements. The final section presents our conclusions.

2. Experiments

2.1. Facilities

Experiments are performed at the University of Michigan in a two-dimensional wave channel with glass bottom and sidewalls. The tank is 35 m long, 0.7 m wide and has a water depth as used of 0.62 m. At one end of the wave tank, wave trains are generated with a servo-controlled wedge-type wavemaker and auxiliary electronics. Two stacks of horsehair mats are placed at the downstream end to help damp the incident waves and minimize reflections. A sketch of the facility is presented in figure 1.

The tank is initially filled with tap water; the water surface is cleaned with a closed-loop system composed of a pump, a reservoir, a filter and connecting hoses. The system can efficiently remove dirt and floating materials from the water surface. When a complete drain and refill is required, the tank is allowed to equilibrate for about one day prior to any measurements to let the water temperature and/or other uncertain factors (e.g. water ageing, Mei 1983) adjust, thus helping to ensure the repeatability of the experiments. The water depth is monitored throughout the experiment and the calm water level variation is limited to less than ± 1 mm.

2.2. Breaking wave generation

Following Perlin *et al.* (1996) and Tian *et al.* (2008), a similar technique is employed to produce dispersive focusing wave trains that lead to wave breaking. Individual

wave steepness during generation remains virtually constant. As demonstrated by Perlin *et al.* (1996), this wave train configuration ensures that the phase speed, as well as the local wave steepness of each wave component in the wave group, changes accordingly when the gain value (i.e. relative voltage of the signal sent to wavemaker) is altered. This method can minimize the presence of premature breaking. Details on the generation of breaking waves using this technique can be found in Perlin *et al.* (1996).

Four wave trains with varying components are implemented. In addition, measurements of the experiments conducted in Tian *et al.* (2008) are included. Figure 2 provides the different wave train structures. Gains are adjusted for each of the wave trains to lead to both non-breaking (5 cases) and breaking waves (12 cases). Detailed wave parameters associated with the wave groups are listed in table 1. Measurements of the non-breaking wave groups are used to compute the non-breaking loss due to surface damping, friction on the sidewalls and the bottom of the tank, and contact-line dissipation (Jiang, Perlin & Schultz 2004), as this non-breaking loss can be important in the determination of energy dissipation (Rapp & Melville 1990; Banner & Peirson 2007; Drazen *et al.* 2008; Tian *et al.* 2008). While it is simple to generate breaking waves using high gain values, significant effort is necessary to find a proper gain and group structure to generate a wave group that leads to a single breaker. In this paper, most of the wave groups that evolve to breaking are characterized with one single plunging breaker, although, in some cases, very limited spilling occurs either upstream, or of less importance downstream.

Breaking waves generated with the aforementioned technique demonstrate strong temporal and spatial repeatability (Tian *et al.* 2008). Observations with high-speed imaging and an accurate synchronization system confirm that the horizontal locations of wave breaking onset vary within only ± 2.5 cm, and that the time is within ± 0.03 s (both better than 0.5 %, considering that breaking usually occurs more than 12 m downstream from the wavemaker and more than 20 s following the initial motion of the wavemaker). A calm water surface (initial condition prior to wave generation) is necessary to achieve the high repeatability; therefore, at least 10 min is allowed between experiments to obtain a near quiescent state, which is also confirmed by visual inspection before each test.

2.3. *Temporal surface elevation measurements*

Capacitance wave probes, transducer power supply, low-pass Krohn–Hite filters, National Instruments data acquisition hardware (i.e. PCI-6034e board and SCB-68 connector block) and Dell PCs are used to record the temporal surface elevations at desired stations along the wave tank. Wave probes are composed of two 25 cm long copper wires, one of which is a sensing wire located within a 1.5 mm diameter glass tube and the other is placed directly in the water. Electronic circuits detect the capacitance between the sensing wire and the water. The sampling rate for each probe is chosen as 100 Hz in this experiment. The low-pass filters are set at 25 Hz. Dynamic calibrations are made before and after each experiment, and are used to convert the measured electric signal to surface elevation. The calibrations confirm that the wave probes exhibit long-term stability. In addition, static calibrations are performed daily to help ensure that no probe malfunction has occurred. To maintain their measurement accuracy, the wave probes are cleaned with alcohol at least twice a day.

An in-line set of three capacitance wave probes are mounted mid-stream (streamwise) from above by a mechanical mount. The distance between adjacent
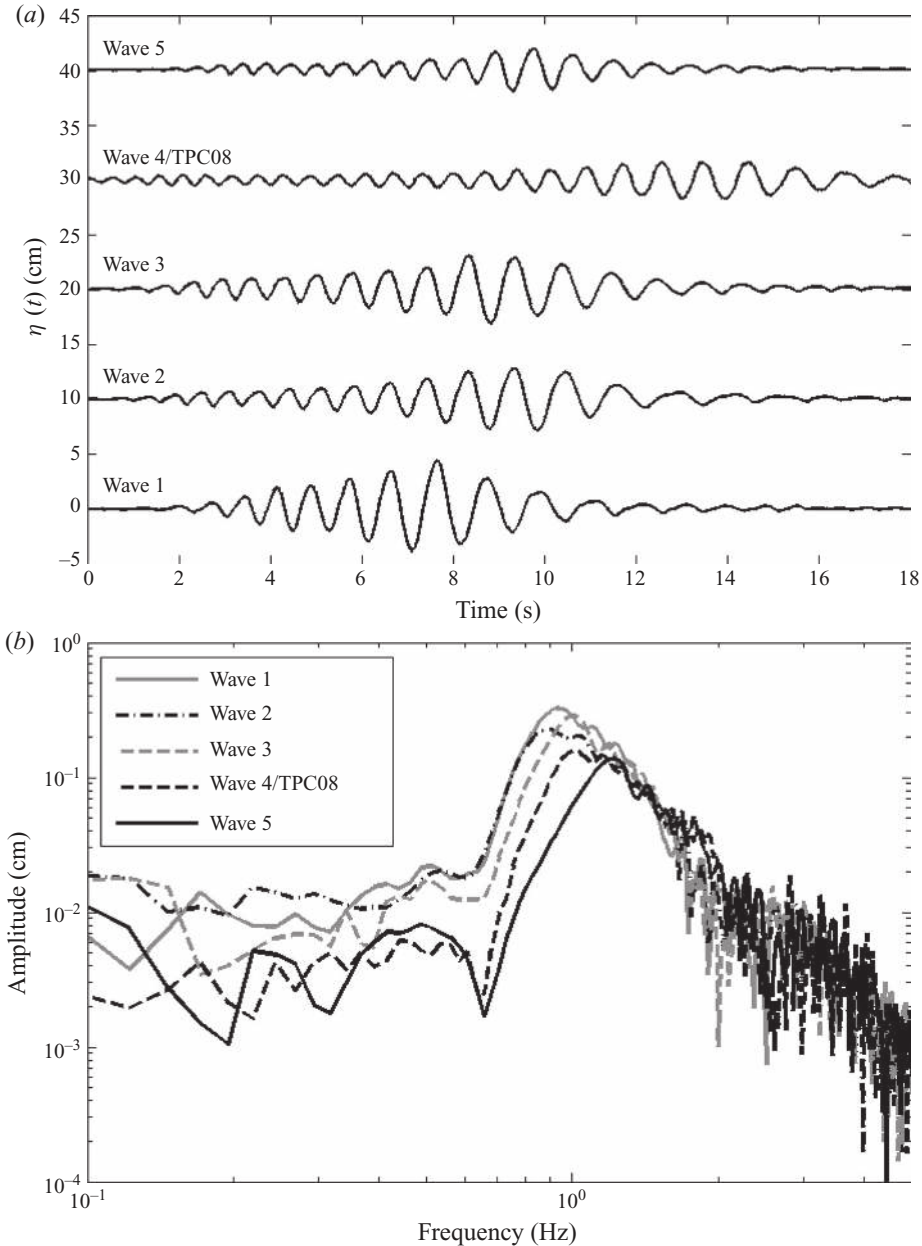
FIGURE 2. Shown are the different wave trains of the various groups. In the figure the non-breaking wave groups measured at the first wave station are presented. In (*a*), for clarity, an increment of 10 cm is applied to separate the measurements vertically. The wave trains have been time shifted so that they can be shown in the same graph. Shown in (*b*) are the amplitude spectra of the wave groups (computed with a 40.95 s measurement, corresponding to 4096 data points).

probes is adjustable and is maintained between 30 and 55 cm. Visual inspections confirmed that surface disturbances by the upstream wave probe(s) have little influence on the downstream one(s). Figure 1(*a*) provides an illustration of the arrangement of the wave probes. With accurate repeatability of an experiment, we chose to obtain

Wave group	Wave ID	f_p (Hz)	$\Delta f/f_p$	S	C_{gs} (m s^{-1})	f_s (Hz)	k_s (rad m^{-1})	E_0 (J m^{-1})	$\Delta E/E_0$	δ_{max} or $\delta_{br} \times 10^3$	k_b (rad m^{-1})	c_b (m s^{-1})	t_{br} (s)	l_{br} (m)	h (m)	$b_b \times 10^3$	$v_{eddy} \times 10^3$ (m^2 s^{-1})
W1	W1G1	0.952	0.307	0.315	0.85	1.019	4.223	—	—	1.08	—	—	—	—	—	—	—
	W1G2			0.381	0.84	1.022	4.247	29.91	0.101	3.39	5.347	1.35	1.11	1.28	0.044	5.91	1.011
	W1G3			0.463	0.84	1.026	4.279	41.62	0.154	6.23	5.878	1.29	1.18	1.30	0.055	14.83	1.196
W2	W2G1	0.903	0.351	0.268	0.86	1.024	4.263	—	—	0.9	—	—	—	—	—	—	—
	W2G2			0.346	0.86	1.021	4.239	21.50	0.084	3.43	5.464	1.34	0.91	1.04	0.038	4.52	0.855
	W2G3			0.413	0.86	1.023	4.255	30.57	0.122	6.09	6.283	1.25	0.99	1.05	0.055	12.15	1.174
	W2G4			0.468	0.86	1.025	4.271	38.94	0.184	6.7	6.203	1.26	1.07	1.19	0.075	20.94	1.651
W3	W3G1	1.025	0.214	0.293	0.79	1.073	4.662	—	—	1.19	—	—	—	—	—	—	—
	W3G2			0.356	0.79	1.073	4.662	18.96	0.088	4.14	5.643	1.32	0.95	1.03	0.032	4.36	0.706
	W3G3			0.442	0.78	1.080	4.721	28.37	0.129	5.76	6.315	1.25	1.00	1.08	0.052	11.94	1.122
	W3G4			0.497	0.78	1.082	4.738	35.16	0.168	6.32	5.911	1.29	1.08	1.15	0.070	15.17	1.499
W4/ TPC08	W4G1	1.025	0.381	0.277	0.71	1.192	5.727	—	—	0.77	—	—	—	—	—	—	—
	W4G2			0.393	0.71	1.192	5.727	12.32	0.090	3.17	5.502	1.33	0.59	0.55	0.033	4.36	0.615
	W4G3			0.544	0.71	1.201	5.813	21.56	0.206	5.06	6.491	1.23	1.08	1.03	0.054	14.4	1.027
	W4G4			0.669	0.70	1.210	5.900	31.20	0.251	6.71	6.670	1.21	1.36	1.43	0.059	21.58	1.234
W5	W5G1	1.245	0.196	0.263	0.66	1.282	6.618	—	—	0.54	—	—	—	—	—	—	—
	W5G2			0.483	0.64	1.295	6.752	10.52	0.186	4.93	7.805	1.12	1.01	0.88	0.031	10.75	0.549

TABLE 1. Summary of the primary wave parameters. f_p: peak wave frequency; Δf: frequency bandwidth based on one-half the maximum energy associated frequencies; S: global wave steepness; C_{gs}: spectrally weighted group velocity; f_s: spectrally weighted wave frequency; k_s: spectrally weighted wavenumber; E_0: total energy just prior to wave breaking; ΔE: energy loss due to wave breaking; δ_{max}: maximum wave breaking criterion parameter, $\delta(t)$, for non-breaking wave groups; δ_{br}: $\delta(t)$ immediately prior to breaking for breaking wave groups; k_b local wavenumber just prior to wave breaking; c_b: breaking wave phase speed; t_{br}: breaking time scale; l_{br}: breaking horizontal length scale; h: falling wave crest/jet height (breaking vertical length scale); b_b: breaking strength parameter; v_{eddy}: estimated eddy viscosity with (3.6).

surface elevation measurements at 33 stations along the tank. For each station, three repeated measurements for each of the wave groups considered are used (i.e. a total of more than 450 runs are achieved). For each measurement, a DC signal synchronized with the initial motion of the wavemaker is recorded and is utilized to align the measurements in time from other runs.

The first station is located 6.81 m downstream of the mean position of the wavemaker (i.e. the wedge's front face intersection with the water). Unless specified otherwise, the distance x is relative to this mean position and time t refers to the initial motion of the wavemaker. The surface elevation measurements at the first station are used to generate initial conditions for our numerical simulations (see §4.2). Based on linear wave theory (LWT), the measurement is first decomposed into 128 Fourier components; then the surface elevation is expressed analytically from a summation of these sinusoidal waves (functions of time and space). Detailed discussions can be found in Tian *et al.* (2008).

2.4. *High-speed imager measurements*

Surface profiles prior to and during active wave breaking are captured by a Phantom high-speed imager (Model 9.1), which has a full resolution of 1632×1200 pixels and can capture images to 144 000 frames per second (f.p.s.) with reduced resolution (1000 f.p.s. at full resolution).

Surface profile measurement has been achieved with high-speed cameras and thin laser light sheets in numerous experiments (Perlin, Lin & Ting 1993; Perlin *et al.* 1996; Duncan *et al.* 1999; Yao & Wu 2005). We initially attempted to use a thin laser sheet as an illuminating source for our tests but abandoned it due to two difficulties encountered. First, laser light sheets usually illuminate a small field of view (to ∼0.5 m) while our study involves measurement windows of lengths to 1.1 m. Second, laser light sheet illumination can be rendered useless by the opacity of the two-phase flow in active wave breaking.

Bonmarin (1989) managed to capture the breaking surface profile with high-power flash lamps and high-speed cameras with a field of view of 1 m. On the other hand, Yao & Wu (2005) and Tian *et al.* (2008) used a backlighting illumination technique to measure surface wave profiles with relatively large field of views.

In this study, we employ a backlighting illumination technique to facilitate the surface profile measurement prior to and during active wave breaking. Figures 1(*b*) and 1(*c*) show the experimental setup. Two high-intensity light sources (each has a maximum output of 2000 W) are seated 30 cm from the corner of the front sidewall and the tank bottom with their mean beam oriented slightly upwards to illuminate the water surface. A reflective and translucent, high-density polyethylene sheet (approximately 6 mm thick) is attached directly to the back sidewall to reflect the light and thus backlight the liquid–gas interface. The imager, equipped with a 28–80 mm focal length Nikon lens, is positioned about 1.5 m from the front sidewall of the tank with its axis oriented slightly downwards for a better image of the field of view (1632×304 pixels), recording at 100 f.p.s. With a precise target of known geometry, the spatial resolution is determined to be 0.683 mm per pixel while the image distortion is shown to be negligible.

Following Tian *et al.* (2008), a synchronization system of light emitting diodes (LEDs) is used to identify simultaneous recorded images and to temporally align measurements from different field of views. This system functions as follows: a DC signal is generated and sent to the LEDs to illuminate them at a specific time relative to the initial motion of the wavemaker. The off–on/on–off status of the LEDs is
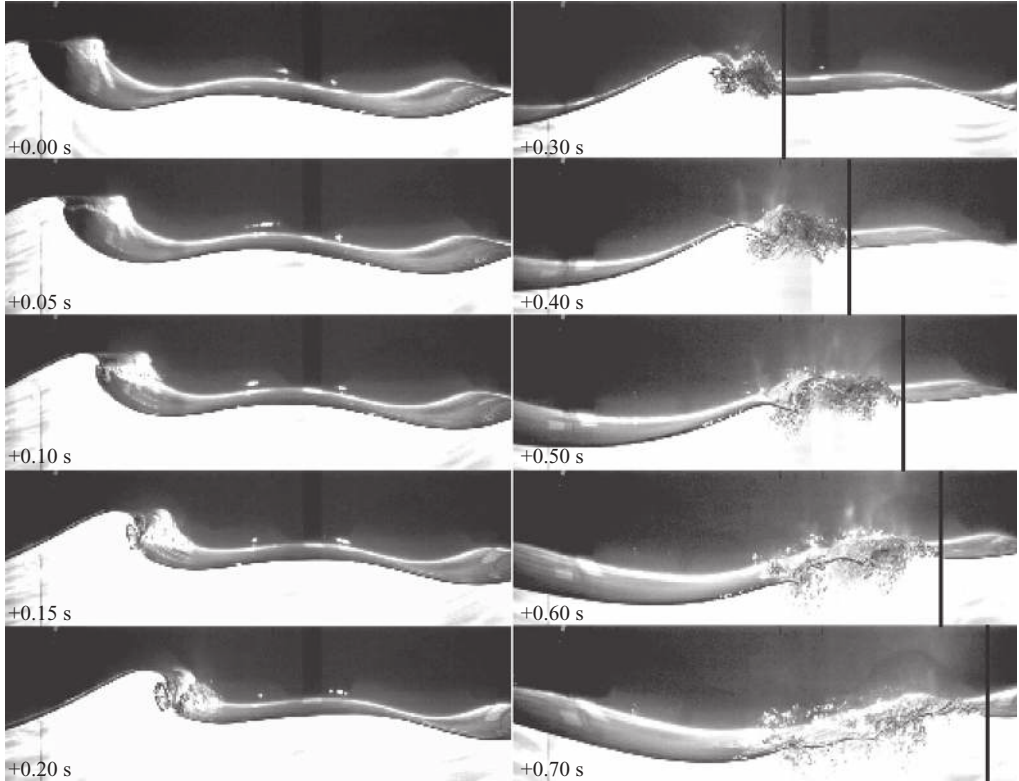
FIGURE 3. Recorded surface profiles during active wave breaking for W4G3. The time sequence is referenced to the first image in the top left photograph. The vertical black bars on the images represent the horizontal location of the surface disturbance front, which is used to define the active breaking time and length scales (see § 3.3.1).

captured with the high-speed imager and applied to determine the start of wave generation. The analysis (Tian *et al.* 2008) has shown that the system can provide sufficient accuracy for our purpose.

As demonstrated by Tian *et al.* (2008), this backlighting technique works well for wave surface profile measurement, especially for a large field of view (about 1.1 m long). A few typical images recorded during active wave breaking are presented in figure 3. As shown, the water surface is defined clearly (the bright interface) and the mean wave profile during active breaking can be identified easily in the recorded images. Careful observations reveal that the amplitude of the capillary waves and the thickness of the contact line effects generated by the water–sidewall interactions are too small (generally within two pixels; less than 1.5 mm) to introduce noticeable perturbations on the recorded surface profiles; therefore, the perturbations of the water–sidewall interactions on the surface profiles are neglected necessarily, although their effects on the total non-breaking dissipation are not negligible (see § 3.2.2). We also note that the wave profile in the absence of breaking can be tracked readily with brightness and contrast adjustments and a MATLAB program; however, when active breaking occurs, the mean profile is extracted manually as a necessity.

3. Experimental results

3.1. *Characteristic wave parameters*

Described below are details of the determination of wave parameters associated with the wave groups and the breaking waves, such as characteristic group velocity, characteristic wave frequencies and wavenumbers, global wave steepness, local breaking wave characteristics and breaking criterion parameter. Unless otherwise noted, most of the wave characteristics associated with the wave group (rather than the wave characteristics associated with wave breaking) are determined from surface elevation measured at the first wave station. Table 1 summarizes these characteristic parameters of the wave groups considered in this study.

3.1.1. *Characteristic group velocity*

It is essential to accurately estimate the characteristic group velocity to compute energy loss from wave probe measurements (Drazen *et al.* 2008). The linear group velocity associated with the centre wave frequency in a wave group is frequently used for this purpose. However, in wave groups with constant wave steepness distribution (e.g. our wave groups have approximately constant-steepness wave spectra based on the first wave probe measurements), wave components with low frequencies have more energy than those with high frequencies. Hence, one may expect that a weighted group velocity rather than a centre frequency group velocity may better characterize the wave group.

Drazen *et al.* (2008) defined a 'spectrally weighted group velocity', C_{gs}, as

$$C_{gs} = \frac{\sum \left(C_{gn} a_n^2 \right) (\Delta f)_n}{\sum \left(a_n^2 \right) (\Delta f)_n}, \tag{3.1}$$

and demonstrated that wave trains propagated at a speed close to this characteristic group velocity. In (3.1), a_n and C_{gn} are the amplitude and linear group velocity of the nth component of the wave train, respectively, and $(\Delta f)_n$ is the frequency difference between components, which is constant here. We note that in the spectral weighting, a_n^2 rather than a_n is used based on an energy argument (i.e. group velocity is the speed of wave energy propagation and a_n^2 is proportional to wave energy).

To evaluate the effectiveness of this spectrally weighted group velocity, C_{gs}, we experimentally measured the group velocity by tracking the wave group maxima. To achieve this, Hilbert analysis is applied to the surface elevation measurements to determine their envelopes, and then the maxima are identified. As can be seen in figure 4, compared with the speed of the wave group maxima, the spectrally weighted group velocity, C_{gs}, appears to be slightly smaller. A nonlinear correction to the group velocity (see Appendix A) is added to C_{gn}, but is found to be too small to appreciably change C_{gs}. Note that C_{gs} remains virtually constant for wave groups with the same input time series but different gains, as shown in table 1. This indicates that the discrepancy should be explained by the nonlinear interaction between different wave components rather than the nonlinear correction to the linear group velocity of each wave component. Despite this small discrepancy, as shown in figure 4, the spectrally weighted group velocity, C_{gs}, indeed provides a good prediction of the wave group propagation speed; on the other hand, the group velocity associated with the centre
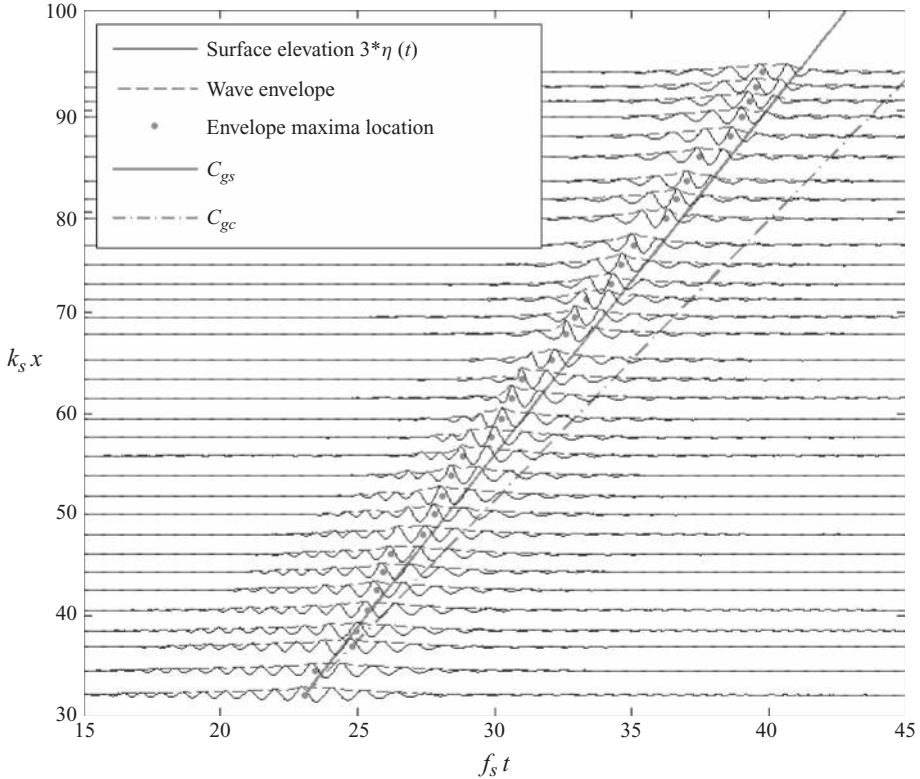
FIGURE 4. Measured time series of surface elevation (W3G3, see table 1 for designations) at various spatial locations. This graph demonstrates that the wave group propagates closer to the spectral weighted group velocity, C_{gs} (solid line); the group velocity associated with the centre wave frequency, C_{gc} (dashed line), significantly underestimates wave group travel speed. f_s and k_s are the characteristic wave frequency and wavenumber, respectively, as shown in table 1. For clarity, the surface elevation is exaggerated by a factor of 3 (i.e. $3^*\eta(t)$ is shown). The spatial locations, $k_s x$, retain their original scale on the vertical axis).

wave frequency that has often been used in the literature provides a significantly smaller and worse prediction, which is consistent with Drazen *et al.* (2008). The group velocity associated with the peak frequency is an alternative, but C_{gs} can be computed more consistently without ambiguity.

We further note that the spectrally weighted group velocity obtained with surface elevation measurements at different wave stations along the tank remains virtually constant for non-breaking wave groups. For breaking wave groups, observations made upstream and downstream of wave breaking exhibit a jump and about a 5–10 % increase in the spectrally weighted group velocity after wave breaking is observed. This increase is caused possibly by the spectral change due to wave breaking, which often dissipates energy in high-frequency wave components (Rapp & Melville 1990; Kway, Loh & Chan 1998) and may introduce a frequency downshift (Lake *et al.* 1977; Melville 1982; Hara & Mei 1991; Trulsen & Dysthe 1997; Dias & Kharif 1999; Tulin & Waseda 1999). On the other hand, this jump is not reported by Drazen *et al.* (2008), who argued that their spectrally weighted group velocity remains unchanged within their experimental accuracy.

3.1.2. *Wave characteristics associated with the wave group*

We now discuss the characteristic wave parameters (i.e. the characteristic wave frequency and wavenumber) associated with our wave groups. The options we used to determine the characteristic wave frequency are: (i) the centre frequency, (ii) the peak frequency and (iii) a spectrally weighted frequency defined in a similar manner as C_{gs}. Among these three trial candidates, the 'spectrally weighted wave frequency' defined by

$$f_s = \frac{\sum (f_n a_n^2)(\Delta f)_n}{\sum (a_n^2)(\Delta f)_n} \tag{3.2}$$

appears to be the best for our wave groups since it provides the best data collapse. In addition, this definition of a characteristic wave frequency is consistent with that of the characteristic group velocity (i.e. both are spectrally weighted).

We further note that the spectrally weighted wave frequency is close to the frequency associated with the spectrally weighted group velocity C_{gs} (i.e. the frequency that provides a group velocity that equals C_{gs} based on LWT and the finite-water-depth dispersion relation; less than 5 % difference for most of the wave groups) and that the latter also produces good collapse of the data. However, to be consistent with the spectral weighting argument (i.e. our wave group's components with low frequencies have more energy than those with high frequencies), the spectrally weighted wave frequency, f_s, is chosen as our characteristic frequency. The linear finite-water-depth dispersion relation is applied to obtain the corresponding characteristic wavenumber k_s and the characteristic wave phase speed c_s, which are termed the 'spectrally weighted wavenumber' and 'spectrally weighted wave phase speed', respectively. We remark that both f_s and k_s remain virtually constant for wave groups with the same input time series regardless of the gain.

3.1.3. *Global wave steepness*

A measure of global wave steepness was first proposed by Rapp & Melville (1990) to measure wave breaking strength. In their experimental study, they generated repeatable focusing wave trains with constant amplitude distribution (i.e. a top-hat wave spectrum) to study breaking waves; their study demonstrated that the global wave steepness parameter, $S_{kc} = k_c \sum a_n$, is strongly correlated with wave breaking strength. Here, a_n is the amplitude of the nth wave component (a total of 32 wave components were specified in their study) and k_c is the wavenumber associated with the centre frequency in their wave group. Subsequent studies (Lowen & Melville 1991; Melville 1994; Drazen *et al.* 2008) drew similar conclusions, although a different definition, $S_{kn} = \sum k_n a_n$, is used for wave groups with constant wave steepness across their wave amplitude spectra.

In this study, we use the surface elevation measured at the first station and Fourier decomposition to compute the global wave steepness. To be consistent with our analysis of the wave group characteristics, the spectrally weighted wavenumber, k_s, rather than the wavenumber associated with the centre frequency of the wave group is used in the computation, $S = k_s \sum a_n$. Note that $\sum a_n$ is the surface elevation at the focusing point according to LWT. Fourier decomposition is applied to the measured signal (windowed for 40.95 s corresponding to 2^{12} points); in fact, this S definition is insensitive to the signal duration as long as all the non-zero surface elevations of the mechanically generated wave packet are included in the determination of the amplitude spectrum, $a(f)$. The computed global wave steepnesses for our groups are listed in table 1.

In the computation of S as well as the other wave group characteristics (i.e. C_{gs} and f_s), we remark that only Fourier components of frequencies in the range [0, 10] Hz (i.e. the first 410 Fourier components, given the fact that the signal is sampled at 100 Hz and windowed for 40.95 s in the Fourier transform) are included. Careful observation of the wave spectra reveals that this frequency range is sufficient to include all meaningful wave components. We further note that all wave group characteristics (i.e. C_{gs}, f_s and $S = k_s \sum a_n$) remain virtually the same even when all Fourier components are considered. On the other hand, this is not the case for the global wave steepness defined as $S_{kn} = \sum k_n a_n$, for which significant variation is found if higher Fourier components are included.

3.1.4. *Local wave characteristics immediately prior to wave breaking*

To characterize the energy dissipation rate due to wave breaking, local wave characteristics have to be determined. With the surface profile measured just before wave breaking, we use the 'local wavenumber' definition proposed by Tian *et al.* (2008), who demonstrated that the wavenumber, $k_b = \pi/|x_{zd} - x_{zu}|$, based on consecutive zero-up (x_{zu}) and zero-down (x_{zd}) crossing points spanning the maximum surface displacement, satisfied Song and Banner's wave breaking criterion (2002). Since the wave breaking process is unsteady, x_{zu} and x_{zd} are determined from the elevation record when the wave crest front becomes vertical. Four to six observations from repeated experiments are used to minimize error. Then the corresponding angular wave frequency, ω_b, is determined using the linear finite-water-depth dispersion relation. The wave speed defined by $c_b = \omega_b/k_b$ (used to estimate the energy dissipation rate due to wave breaking in §3.3.2) is termed the 'breaking wave phase speed', c_b. The resulting c_b are listed in table 1.

We compared the wave characteristics associated with the wave group (i.e. f_s, k_s and c_s) to the local wave characteristics just prior to wave breaking (i.e. f_b, k_b and c_b) to examine the possibility of definite correlations among them. As shown in figure 5, it is found that the 'local wave steepness', S_b, prior to wave breaking defined by $S_b = k_b \sum a_n$ is roughly a linear function of S. Any data scatter can be attributed to the fact that each wave group has different bandwidth since S_b is expected to be a function of S and bandwidth, although its dependence on bandwidth is found to be weak (see our discussion in §3.2.3). For our wave groups, it is found that $S_b = 1.237S$. This implies that a wave group of relatively large global wave steepness increases in slope immediately before wave breaking occurs, which might lead to more violent wave breaking, resulting in larger energy dissipation. In addition, the local wave speed and the local wavenumber can be approximated as $c_b/c_s = 0.9 \pm 0.1$ and $k_b/k_s = 1.25 \pm 0.25$, respectively.

3.1.5. *Wave breaking criterion parameter*

Banner & Peirson (2007) and Tian *et al.* (2008) reported that their 'wave breaking criterion parameter' immediately prior to breaking onset, δ_{br}, is strongly correlated with the wave breaking strength. First, a parameter $\delta(t)$ is defined as $\delta(t) \equiv [D\langle\mu(t)\rangle/Dt]/\omega_c$, where ω_c is the centre angular wave frequency, $\langle\mu(t)\rangle$ denotes the mean of the upper and lower envelopes of $\mu(t)$ and $\mu(t) = [E_{max}/\rho g]k^2$. E_{max} is the local wave energy density at the maximum surface displacement (see Song & Banner 2002 for details). In this study (including data from Tian *et al.* 2008), δ_{br} is set $\delta(t)$ at breaking except that in the calculation of $\delta(t)$, the characteristic wave frequency ($\omega_s = 2\pi f_s$) instead of ω_c is used. This choice reduces data scatter for our experimental measurements. As illustrated in table 1 and also in Tian *et al.* (2008),
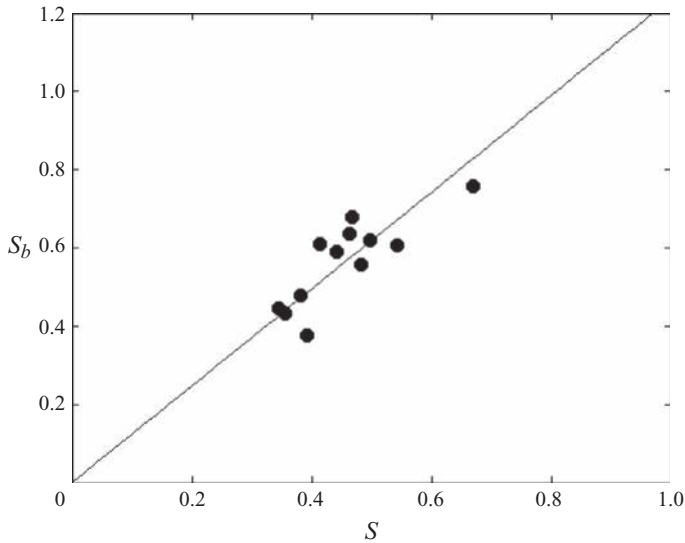
FIGURE 5. Global wave steepness, S, versus local wave steepness, S_b. The solid line represents a linear least-squares fit: $S_b = 1.237S$.

this parameter with threshold $\delta_c = (1.4 \pm 0.1) \times 10^{-3}$ distinguishes wave groups that lead to wave breaking from those that do not.

It is of interest whether there is any correlation between S_b (or S) and Song and Banner's wave breaking criterion parameter, δ_{br}. Banner & Peirson (2007) made indirect comparisons between S and δ_{br} by correlating both parameters to the total mean energy loss. They found that both δ_{br} and S increase in general as the total mean energy loss rises. As S_b measures the local wave slope and $\mu(t) = S_b^2$, the wave breaking parameter of Song & Banner (2002) can be approximated by

$$\delta_{br} = BS_b^2 \frac{\omega_b}{\omega_s}, \tag{3.3}$$

where $\omega_b = 2\pi f_b$ and B is a proportionality constant. As shown in figure 6, (3.3) is indeed a good approximation to δ_{br} and, considering that S_b is linearly correlated with S, the wave breaking parameter δ_{br} can be roughly approximated by $\delta_{br} \sim \omega_b S^2 / \omega_s$. We will further examine the applicability of S_b and δ_{br} as wave breaking strength indicators and include a detailed discussion in §3.2.3.

3.2. *Energy loss*

3.2.1. *Estimation of total energy*

Following Drazen *et al.* (2008) and Tian *et al.* (2008), total energy is estimated based on surface elevation measurements. The approximate total energy is obtained by time integration of the linear theory energy flux, $F(x, t) = \rho g C_{gs} \eta^2(x, t)$, at fixed spatial locations. Here, $F(x, t)$ is the energy flux, ρ is the water mass density, g is the gravitational acceleration, C_{gs} is the spectrally weighted group velocity computed with surface elevation measurements at the first wave station and $\eta(x, t)$ is the measured surface elevation.

This simplification based on linear theory in estimating the energy flux is valid except where nonlinearity becomes significant (e.g. close to wave breaking or focus
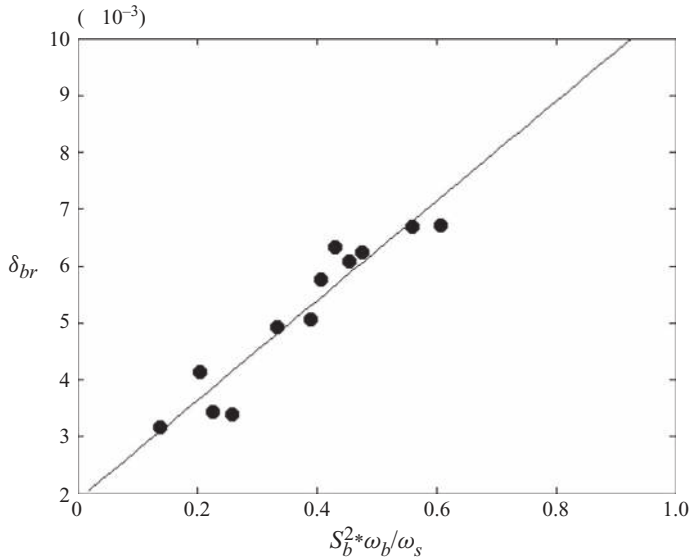
FIGURE 6. Correlation between S_b and δ_{br}. The solid line represents a linear least-squares fit and the slope is 8.77×10^{-3}.

points), and it is accurate to the second order, $O[(ka)^2]$ (Rapp & Melville 1990), where 'a' is the wave amplitude. Since our measurement is initiated from quiescent conditions (before wave groups arrive) and continues through quiescent conditions (after wave groups pass), the time integration of the energy flux provides the total energy, $E(x) = \{F(x, t)\}$. Here, $E(x)$ is the total energy and $\{\cdots\}$ denotes integration with respect to time.

Figure 7 presents the total energy as a function of position, x. Obvious in the figure are data oscillations superposed on a general decay trend. Similar observations were also made in previous studies (e.g. Rapp & Melville 1990; Kway *et al.* 1998; Banner & Peirson 2007), but have not been addressed explicitly. The decreasing trend of the total energy as a function of space is mainly due to surface damping, contact-line dissipation (Jiang *et al.* 2004), friction by tank sidewalls and the bottom, and, most importantly, wave breaking (for breaking wave groups only). On the other hand, the smaller oscillations in regions far from wave focusing/breaking are mainly due to measurement error; meanwhile, the oscillations in wave focusing/breaking regions (where nonlinearity becomes prominent) may be partially attributed to failure of the linear assumption in estimation of the total energy. (In figure 7, note that the oscillations of $E(x)$ prior to breaking increase as the initial wave group energy flux increases.)

Nevertheless, even for the non-breaking case, a significant decrease of the energy is observed and is likely to be due to viscous dissipation and contract-line dissipation. Therefore, non-breaking energy loss has to be estimated before energy loss due to wave breaking is computed.

3.2.2. *Non-breaking energy loss*

We assess energy loss due to viscous dissipation and contact-line damping with experimental measurements of non-breaking wave groups and previous theoretical analysis for viscous losses (Lamb 1932; Mei 1983; Tulin & Waseda 1999),
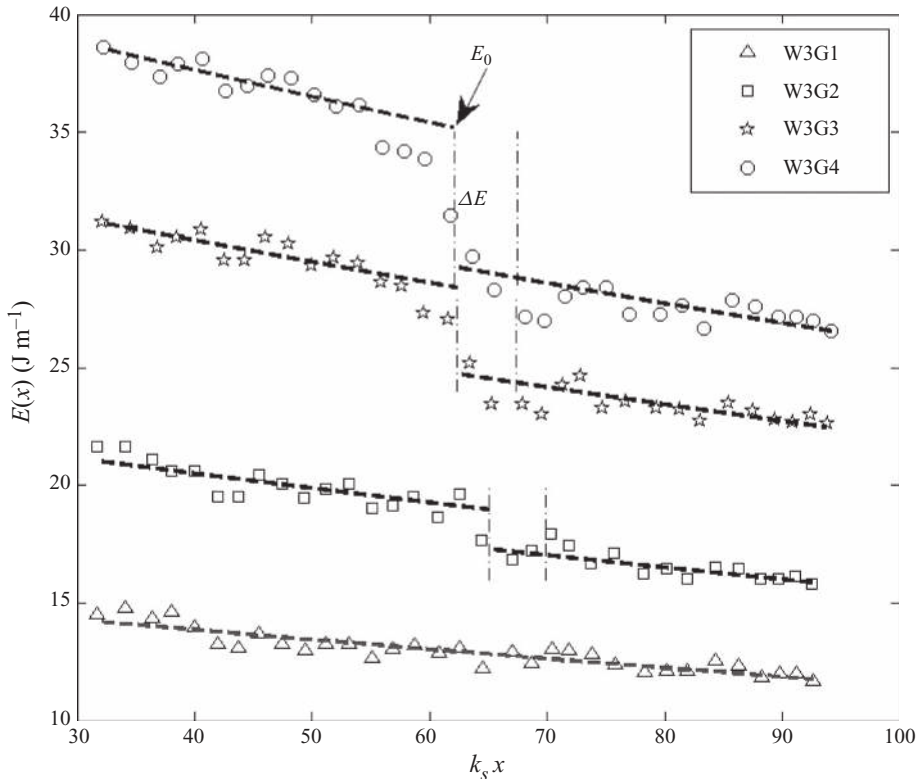
FIGURE 7. Estimation of energy loss due to friction, contact-line damping and wave breaking, shown only for wave 3. The thick dashed lines are the exponential best fits; the vertical dashed–dotted lines denote the active breaking length scale. Non-breaking losses are estimated from the exponential fit of the non-breaking wave measurements (lowest, W3G1). E_0 is the estimated total energy just prior to wave breaking based on the exponential fit; ΔE is the estimated energy loss due to wave breaking, both shown only for W3G4.

which demonstrate that the energy decay rate due to viscosity is exponential, $E = E_{first} \exp(-\sigma x)$. Here, σ is the spatial decay rate due to bulk viscosity and boundary layers in the free surface, sidewalls and bottom, and E_{first} is the total energy at the first wave probe location.

An exponential best fit in the least-squares sense is applied to the measured total energy of the non-breaking case to obtain the decay rate. As shown in figure 7, the exponential best fit is close to a straight line. Therefore, the decay may be approximated by a linear decrease (as in figure 15 of Tian *et al.* 2008) or by a quadratic least-squares best fit (as in figure 6 of Banner & Peirson 2007) over a short distance. Also visible in figure 7 is that roughly 15 % of the total energy is dissipated at a distance of 10 characteristic wavelengths. Significant energy loss was also reported by Banner & Peirson (2007), who showed 20 % of mean wave energy loss in 37 wave periods. Therefore, viscous energy dissipation is significant and should be taken into account while determining energy loss due to wave breaking.

For the wave groups considered in this study, the exponential decay rate, σ, estimated with the exponential best fit is $O(0.01)$, which is as much as 40 % greater than the LWT prediction (Lamb 1932; Mei 1983; Tulin & Waseda 1999).

This discrepancy is attributed to the nonlinearity and, more importantly, the highly dissipative capillary waves and contact lines generated by the water–sidewall interactions (Perlin & Schultz 2000; Jiang *et al.* 2004).

3.2.3. *Energy loss due to wave breaking*

The energy loss due to wave breaking is defined as the total energy loss minus the non-breaking energy dissipation. First, measurements upstream and downstream of wave breaking are fitted with the dissipation rate of the non-breaking case, respectively, to account for the non-breaking loss. Then, the energy dissipation due to wave breaking is determined from the step change between the upstream and the downstream best fits at the point where wave breaking initiates, as illustrated in figure 7. Details can be found in Banner & Peirson (2007) and Tian *et al.* (2008). We note that the best fits exclude measurements near and in the active breaking region, where total energy estimation using LWT contains considerable error due to strong nonlinearity. An alternative approach to estimate energy loss would be the control volume approach suggested by Rapp & Melville (1990), where the total energy loss can be determined by the difference of total energy fluxes in and out of the control volume.

We remark that we use the spectrally weighted group velocity computed at the first wave station to estimate the total energy and total energy loss due to wave breaking. This is done for consistency with other wave characteristics even though we observed an increase in the group velocity after wave breaking, as described in §3.1.1. By doing so, the energy loss and energy loss rate may be slightly overestimated since the post-breaking energy proportional to the group velocity is underestimated.

The energy loss due to wave breaking as a function of S and δ_{br} is presented in figure 8. When non-dimensionalized by $\rho g / k_s^3$, both the estimated total energy prior to wave breaking, E_0, and the estimated energy loss due to wave breaking, ΔE, are very well correlated with the global wave steepness, S. Therefore, the normalized energy dissipation ($\Delta E/E_0$) closely correlates with S, as in figure 8(*b*). The relationship can be well approximated with a linear least-squares fit, as illustrated in the figure. Alternatively, both E_0 and ΔE are well correlated with the local wave steepness, S_b.

Both E_0 and ΔE normalized with respect to $\rho g / k_s^3$ are expected to be functions of S and $\Delta f/f_s$ from dimensional analysis (Drazen *et al.* 2008, §2.1), where Δf is the frequency bandwidth associated with one-half the maximum energy wave frequencies, as shown in table 1. However, our results indicate that the dependence of the local energy and the energy loss on the bandwidth $\Delta f/f_s$ is weak and will be neglected. The weakness of the effect might be explained by the fact that wave breaking in our experiments is achieved mainly by linear superposition rather than a nonlinear mechanism such as the Benjamin–Feir instability where the bandwidth plays a crucial role.

On the other hand, $\Delta E/E_0$ is not well correlated with δ_{br}, while the normalized energy loss due to wave breaking, in general, increases with δ_{br}, as shown in figure 8(*c*). A better correlation can be found between $\Delta E/E_0$ and $(\delta_{br}\omega_s/\omega_b)^{1/2}$, which is proportional to S_b, as discussed in §3.1.5. Our results are somewhat inconsistent with Banner & Peirson's study (2007), in which δ_{br} was shown to have a better correlation with the energy dissipation due to wave breaking. We remark that both S and δ_{br} defined in this study are different from those of Banner & Peirson (2007).

It is worthwhile to make two additional comments regarding figure 8. The first one is regarding the global wave steepness threshold, S_0, which indicates incipient wave breaking. Our results in table 1 show that the threshold resides in the range [0.31, 0.35].
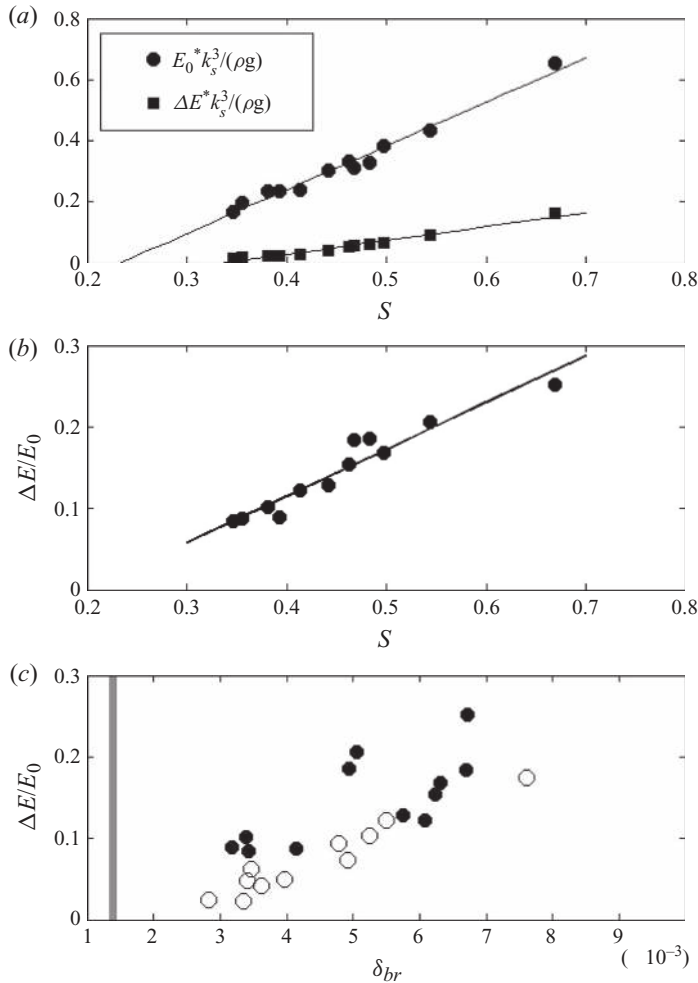
FIGURE 8. Normalized energy loss versus S and δ_{br}. Banner & Peirson (2007) data (open symbols in the figure) are reproduced for comparison. The solid lines in (a) and (b) represent linear least-squares fits. The thick vertical line in (c) illustrates the threshold, $\delta_c = (1.4 \pm 0.1) \times 10^{-3}$, for wave breaking onset, as discussed in Song and Banner (2002) and Tian *et al.* (2008).

From figure 8(a), ΔE can be approximated by $\Delta E / (\rho g / k_s^3) = 0.445(S - 0.339)$ and, therefore, S_0 is roughly found to be 0.339 for which $\Delta E = 0$. As described in § 3.1.4, $S_b = 1.237S$ and, therefore, the local wave slope criterion for incipient wave breaking can be estimated by $(S_b)_0 = 0.419$, which is slightly smaller than the maximum slope of 0.441 for deep water Stokes' waves.

Previously, Rapp & Melville (1990) reported that incipient breaking waves are associated with S_0 between 0.22 and 0.25. Banner & Peirson (2007) observed incipient breaking waves with S_0 as small as 0.12, much lower than previously reported even with viscous damping taken into account. (Note that Banner & Peirson 2007 obtained S with measurements just prior to breaking onset, and they reported a mean energy loss of 20 % due to viscous damping. This energy loss translates to an amplitude loss around 10 %. Therefore, their S could be ∼10 % larger for their upstream

measurements.) In addition, the measurements by Drazen *et al.* (2008) show that wave breaking does not occur until S becomes approximately 0.3. We remark that this variation in S_0 may be mainly due to different definitions of S and may be partially related to different wave trains (i.e. wave spectrum shape). Although our definition of S well predicts the total energy loss due to wave breaking, the applicability of S as a universal indicator of wave breaking onset needs to be further explored due to the variation of S_0 in different laboratory studies. In addition, we need to consider that the friction on the tank side walls and bottom and contact line dissipation modify S as wave groups approach breaking. This fact may also limit the application of S for breaking onset prediction, as S is determined at some arbitrary location prior to breaking in laboratory experiments.

Alternatively, the local wave steepness, S_b, might be a better parameter to understand wave breaking. Although the relationship between S and S_b might depend on particular wave trains, the local wave characteristics prior to breaking might be more universal. However, S_b may not be known accurately in advance of the actual breaking event.

The second issue is the different level of total energy loss due to wave breaking. For a comparable δ_{br}, our energy dissipation level is generally greater than that reported by Banner & Peirson (2007), whose wave groups commonly have multiple spilling breakers. Since our wave groups are essentially single plunging breakers, the discrepancy might be associated with some intrinsic difference between spilling and plunging breakers. However, a recent study by Drazen *et al.* (2008, figure 14) demonstrated that spilling and plunging breakers may have the same breaking strength (i.e. b). Regardless, the cause of the discrepancy in energy dissipation is not yet well understood.

3.3. *Energy dissipation rate due to wave breaking*

3.3.1. *Time and horizontal length scales of wave breaking*

In this section, we discuss the time and length scales associated with active wave breaking in laboratory studies. These scales will be used to estimate the energy dissipation rate under the assumption that the dissipation rate is constant throughout the breaking process.

Accurate estimation of energy loss rate defined by the energy loss per unit time during wave breaking undoubtedly requires accurate estimation of the dissipation time scale, which should be obtained with detailed velocity field measurements during active wave breaking. However, this measurement proves extremely difficult due to the two-phase flow opacity, bubble scattering in the active breaking crest (Perlin *et al.* 1996) and the large field of view needed. To our knowledge, the dissipation time scale for energy loss due to active wave breaking based on robust and reliable measurements has not been reported. Information available for the time scale are the measurements by Rapp & Melville (1990), who reported that 90 % of the total energy loss occurs within four wave periods after incipient breaking. In addition, based on their numerical study, Chen *et al.* (1999) reported that 80 % of the total energy loss occurred within three wave periods.

In this study, the 'breaking time scale', t_{br}, used to estimate energy loss rate is defined as the time from when the wave crest begins to fall to the time when the surface disturbance front is no longer obvious; the horizontal location of the surface disturbance front is represented by the vertical bars in figure 3. It is somewhat subjective when the surface disturbance front is no longer obvious; repeated trials show that the variation of the measured time scale is limited to within ± 0.02 s (i.e. less
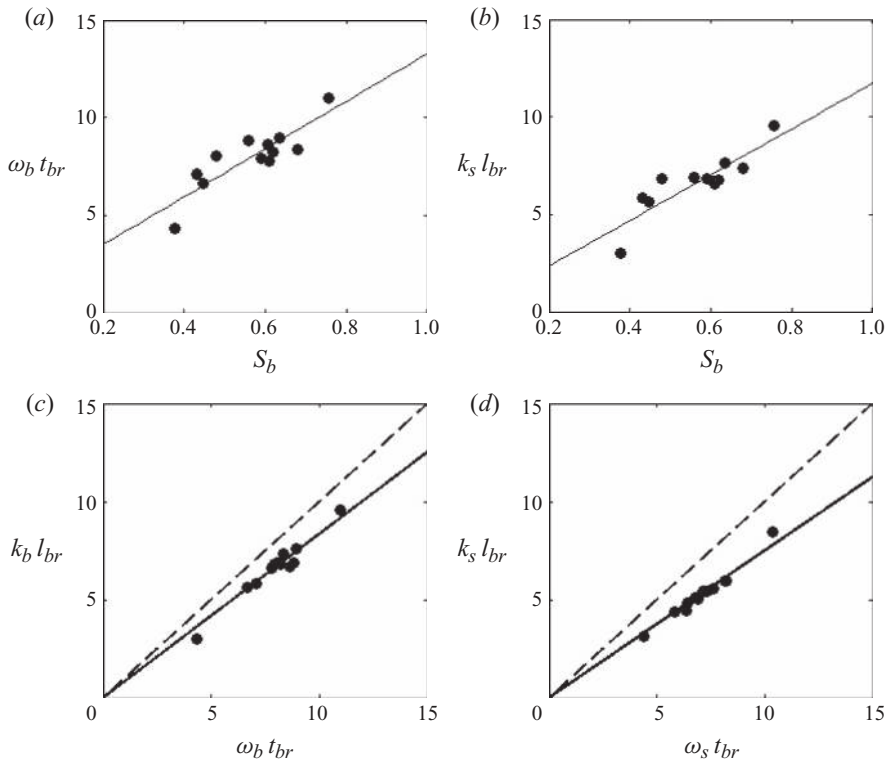
FIGURE 9. Time scale t_{br} and length scale l_{br} associated with active wave breaking. ω_b and k_b are the wave frequency and the wavenumber associated with the breaking wave (see §3.1.4 for details). ω_s and k_s are the spectrally weighted wave frequency and wavenumber. Solid lines represent linear least-squares fits. In (*c*), the dashed line illustrates the characteristic wave speed, c_b, based on local wavenumber, k_b, measurement; the solid line represents the estimated horizontal breaking crest speed as $u_{br} = 0.836c_b$. And in (*d*), the dashed line represents the characteristic wave speed, c_s, based on the spectrally weighted wave frequency ω_s; the solid line represents the estimated horizontal breaking crest speed as $u_{br} = 0.750c_s$.

than 5 % considering this time scale is of the order of 1 s for our wave groups). These time scales are presented in figure 9(*a*). The dissipation time scale is of the order of one characteristic wave period ($2\pi/\omega_b$). For breaking from wave groups with similar spectral shape and phase, the dissipation duration increases as breaking intensifies, or, equivalently, as S_b increases. The trend is consistent with that in Drazen *et al.* (2008).

Also shown in figure 9 is the 'horizontal breaking length scale', l_{br}, which is defined as the distance from incipient breaking to where the obvious surface disturbance front ends. As seen in figure 9(*b*), l_{br} increases as wave breaking intensifies. In the short time, t_{br}, the 'whitecap' coverage (l_{br}) can extend as far as one and a half characteristic wavelengths ($2\pi/k_b$) for the most violent breaking while other plunging breakers have length scales around one characteristic wavelength, which is consistent with the dye patch experiments of Rapp & Melville (1990). In general, both t_{br} and l_{br} depend linearly on S_b when they are non-dimensionalized with respect to ω_b and k_b. This indicates that the breaking process is more violent as the local wave slope increases.

Since the horizontal length scale, l_{br}, is essentially the distance that the apparent surface-disturbance front travels in t_{br}, the length and the time scales are expected

to be related by the 'horizontal breaking wave crest speed', $u_{br} = l_{br}/t_{br}$. Note that the breaking crest speed is less than the linear phase speed of the breaking wave, c_b, defined as $c_b = \omega_b/k_b$ in §3.1.4. Based on the breaking time and horizontal length scales, we can estimate the ratio of u_{br} to c_b, represented by the slope of the solid line in figure 9(c). The estimation of $u_{br} \sim 0.836c_b$ generally agrees with that reported by Melville & Matusov (2002), but is greater than that reported by Banner & Peirson (2007). It is interesting to note from figure 9(d) that u_{br} can be well estimated in terms of the spectrally weighted wave phase speed as $u_{br} \sim 0.750c_s$.

3.3.2. *Rate of energy loss due to wave breaking*

Based on dimensional analysis, the 'energy dissipation rate', ε, scales to the fifth power of a characteristic speed, U

$$\varepsilon = b\rho\, U^5/g, \tag{3.4}$$

where b is a dimensionless 'wave breaking strength parameter' (Duncan 1981; Melville 1994; Banner & Peirson 2007; Drazen *et al.* 2008; Gemmrich *et al.* 2008), which might depend on global wave parameters, such as the global wave slope and the bandwidth. This equation relates the kinematics and the dynamics of wave breaking by using a wave breaking strength parameter and is expected to approximate the energy dissipation rate due to wave breaking in spectral modelling of ocean waves (Phillips 1985; Phillips *et al.* 2001; Melville & Matusov 2002; Gemmrich *et al.* 2008).

Both laboratory experiments and field measurements have been conducted to quantify the breaking strength parameter (Duncan 1981, 1983; Phillips 1985; Thorpe 1993; Melville 1994; Phillips *et al.* 2001; Melville & Matusov 2002; Banner & Peirson 2007; Drazen *et al.* 2008; Gemmrich *et al.* 2008). The reported breaking strength parameter varies over a wide range (more than two orders of magnitudes), and generally, estimation based on field data is much less than that from well-controlled laboratory experiments. The discrepancy remains unresolved (Gemmrich *et al.* 2008).

It would be beneficial if a universal constant could be found for b, independent of wave parameters, for a particular choice of U, but it is unlikely that one exists since for a given wave phase speed, there can be a wide range of breaking intensities. It is therefore of interest to find a form of b that well correlates with the characteristic wave parameters. Depending on the choice of the characteristic velocity, different definitions for b have been proposed. For example, Duncan (1981, 1983) used the breaking wave crest velocity, u_{br}, and defined the corresponding wave breaking strength parameter, b_{br}. To facilitate its application to the estimation of the energy-dissipation rate of a wave spectrum, in which wave speed, c, corresponding to Fourier wave components is employed commonly, Banner & Peirson (2007) proposed to use the breaking wave phase velocity, c_b, for which b_b can be determined. As discussed in §3.1.4, c_b exhibits an almost linear relationship with the breaking wave crest velocity, $u_{br} \sim 0.836c_b$, and b_b can be estimated as $b_b \sim 0.836^5 b_{br} = 0.408b_{br}$. This is consistent with Banner & Peirson (2007), who showed that b_b is approximately one half of b_{br}.

A straightforward method to evaluate b is based on the estimation of total energy loss and direct measurements of the active breaking time (Melville 1994; Drazen *et al.* 2008). First, the energy dissipation rate is estimated as $\varepsilon = -\Delta E/t_{br}$. The breaking strength parameter is then evaluated from (3.3) as $b = \varepsilon g/\rho U^5$. This method involves only local wave breaking characteristics (e.g. local energy 'jump' and active breaking time) and is adopted here to compute b.

Banner & Peirson (2007, Appendix A) proposed an alternative method to estimate b based on mean energy loss and mean energy propagation (i.e. temporal and spatial
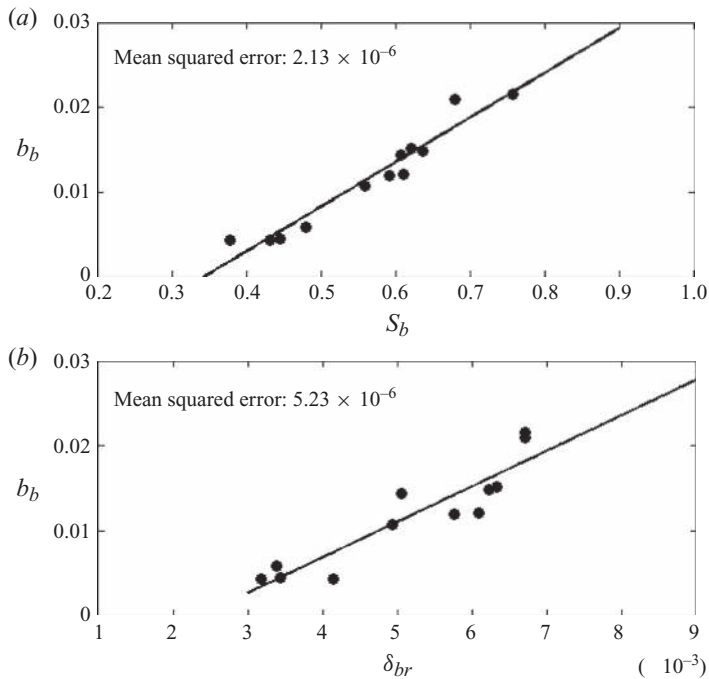
FIGURE 10. Normalized energy dissipation rate versus S_b and δ_{br}. Solid lines represent linear least-squares fits.

transfer), $b = gC_g\Delta[\hat{E}]/c_b^5$. Here, $\Delta[\hat{E}]$ is the mean energy density loss, $[\cdots]$ denotes average over a wave group and $\hat{E} = g\eta^2$. This method provides an estimation of b without evaluating the breaking wave time scale t_{br}. We note that the application of Banner & Peirson's (2007) estimation scheme to our breaking waves is somewhat arbitrary as there is ambiguity in choosing the average period to obtain the mean energy loss. Therefore, their method is not adopted here.

Results of our measurements are given in figure 10. Obvious in the figure is the strong correlation between S_b and b_b, which implies that the energy dissipation rate increases as the local wave slope increases. As shown in figure 10(b), the breaking strength parameter, b_b, is also correlated with δ_{br}, as expected: a larger δ_{br} is associated with a larger dissipation rate, but the correlation between S_b and b_b appears to be stronger than that between δ_{br} and b_b. Figures 8 and 10 imply that S_b is a more appropriate parameter to predict both energy loss and energy loss rate due to wave breaking for our wave groups than is δ_{br}. As mentioned before, this is inconsistent with the results of Banner & Peirson (2007), who observed that δ_{br} is a more fundamental parameter to characterize both energy loss and energy loss rate due to wave breaking for their wave groups. The discrepancy is mainly attributed to different wave groups.

Our estimated wave breaking strength parameter is of the same order of magnitude as Melville (1994), but is about one order of magnitude larger than that of Banner & Peirson (2007). Therefore, proper comparison with the latter requires additional attention to the wave group parameters. Typical lengths of our wave group are $O(10\text{ m})$ and characteristic group velocities are $O(1\text{ m s}^{-1})$, which reduces our wave breaking strength parameter one order of magnitude if Banner & Peirson's method is used for the calculation. Therefore, our results are generally of the same order of

magnitude as Banner & Peirson's (2007), subject to proper data interpretation. In comparison to measurements by Drazen *et al.* (2008), our energy dissipation rate is about one third to one half of theirs (for a comparable S–S_0). This discrepancy is mainly attributed to the relative short time scale used in their estimation. Different wave group structures may also contribute to this disparity. In addition, their data (figures 13 and 14 in Drazen *et al.* 2008) appear to have much more scatter than ours. The scattering may be due to the fact that they used the wave phase speed and wavenumber based on the centre frequency, c_c and k_c, rather than c_b and k_b, in their dissipation rate parameterization.

3.4. *Eddy viscosity*

It is our intent to model eddy viscosity to determine the energy dissipation due to deep water breaking waves. For simplicity, a constant eddy viscosity is assumed throughout the breaking process. Dimensional analysis served as a simple yet effective way to obtain the proper time and length scales for the eddy viscosity estimation.

For a plunging breaker, we believe that the active breaking time, t_{br}, and the horizontal breaking length, l_{br}, are the proper time and horizontal length scales, respectively. As for the vertical length scale, Rapp & Melville (1990) suggested that the breaking wave penetration depth, D, is comparable with the characteristic length scale of the turbulence generated by wave breaking; therefore, D may be employed as the vertical length scale in the analysis. Our experiments provide no measurement of the penetration depth. However, the penetration is caused mainly by the falling wave crest/water jet. Therefore, a large falling wave crest/water jet height would introduce a large breaking penetration depth, which is confirmed qualitatively with the high-speed imager in our experiments. Thus, the falling wave crest/water jet height, h, as defined in Drazen *et al.* (2008), is used as the vertical length scale in this analysis.

For the turbulent viscous flow in breaking waves, we assume that the energy dissipation rate can be expressed as in Phillips (1977, §3.4) by replacing the kinematic viscosity with eddy viscosity, v_{eddy}, as

$$\frac{\mathrm{d}E}{\mathrm{d}t} = -\frac{1}{2}\rho v_{eddy} \int \left(\frac{\partial u_i}{\partial x_j} + \frac{\partial u_j}{\partial x_i}\right)^2 \mathrm{d}A \sim \rho v_{eddy} \frac{c_b^2}{h^2} h l_{br}, \tag{3.5}$$

where A represents an area over which large vorticity of $O(c_b^2/h^2)$ is induced by breaking waves and is estimated by $h l_{br}$. In addition, we choose to estimate the energy dissipation rate, $\mathrm{d}E/\mathrm{d}t$, with $\rho c_b^2 l_{br}^2/t_{br}$ based on dimensional analysis. When combined with this estimation, (3.5) yields the following estimation of eddy viscosity:

$$v_{eddy} = \theta h l_{br}/t_{br}, \tag{3.6}$$

where θ is a proportionality coefficient and remains to be determined.

Alternatively, the eddy viscosity can be represented by $v_{eddy} \sim ul$ (Rapp & Melville 1990), where u is an integral velocity scale and l is an integral length scale. Based on the dye patch experiments by Rapp & Melville (1990), the integral length l is roughly comparable with the breaking wave penetration depth. However, as mentioned before, we choose to use the falling wave crest height, h, as the vertical length scale. As for the integral velocity, u, it is considered to be a fraction of the breaking wave phase speed, $u = \chi c_b$ (Melville 1994), where χ is a numerical constant in the range [0.1, 0.17] in his analysis, depending on the breaking strength (see Appendix C). Then,
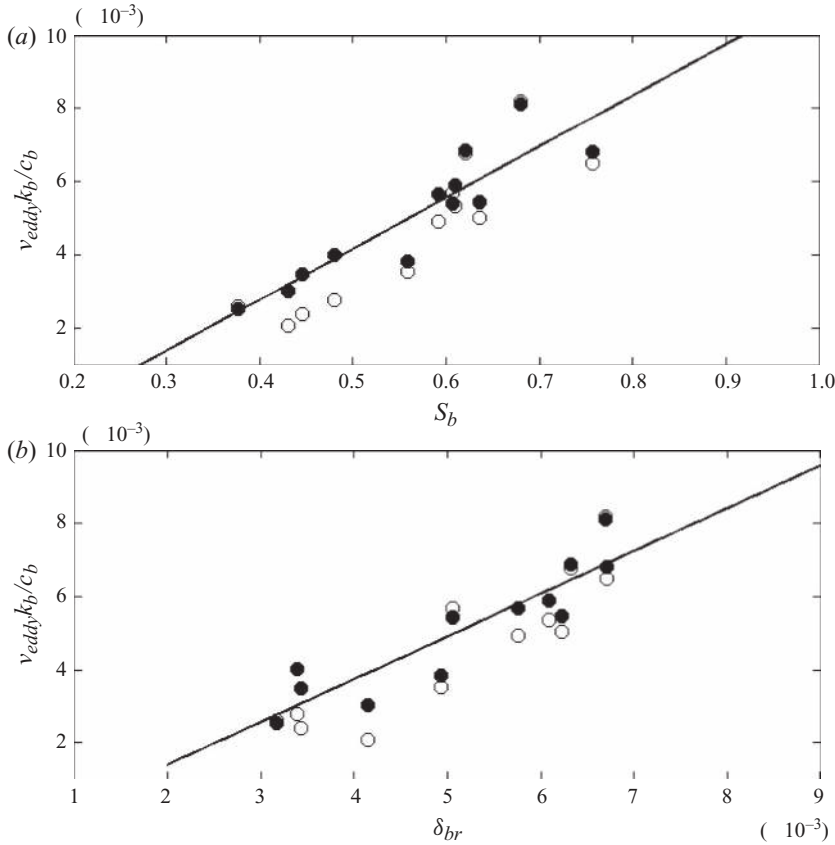
FIGURE 11. Eddy viscosity as a function of the wave breaking strength is presented. Solid symbols denote estimations using (3.6) and open symbols using (3.7). The two equations provide estimations close to each other. In this study, estimations with (3.6) are used in the numerical simulations. Solid lines represent linear least-squares fits (only estimations with (3.6) are included in the best fits).

from $\nu_{eddy} \sim ul$, the eddy viscosity is estimated as

$$\nu_{eddy} = \theta' ul = \theta' \chi c_b h, \tag{3.7}$$

where θ' is a proportionality coefficient and remains to be determined. Note that (3.7) is consistent with (3.6) since l_{br}/t_{br} in (3.6) is the horizontal breaking wave crest speed, u_{br}, which is found in §3.3.1 as a fraction of the breaking wave phase speed, c_b.

Eddy viscosities associated with different wave groups are estimated using the experimental measurements and (3.6) and (3.7) (the proportionality coefficients in the equations are determined as $\theta = 0.02$ and $\theta' = 0.10$ for our wave groups; see §4.2 for details). As presented in figure 11, the two equations provide similar estimations that are of the order of 10^{-3} m^2 s^{-1}. We remark that the kinematic viscosity of water is $O(10^{-6}$ m^2 s$^{-1})$. Also, as can be seen in the figure, the eddy viscosity increases as wave breaking intensifies (i.e. S_b and δ_{br} increase). In the following section, the estimated eddy viscosities are implemented in numerical simulations to model energy dissipation due to wave breaking.

4. Eddy viscosity parameterization and numerical simulations

4.1. *Eddy viscosity parameterization*

Ruvinsky, Feldstein & Freidman (1991) presented a system of coupled equations for weakly damped surface waves and used them to study capillary-gravity ripples riding on steep gravity-capillary waves. The derivation of the coupled equations involved separating the potential and the vortical components of the flow: $\boldsymbol{u} = \nabla\phi + \boldsymbol{u}'$ with $\boldsymbol{u}' = \nabla \times (-\psi)\boldsymbol{j}$. Here, ϕ is the velocity potential; $\boldsymbol{u} = (u, w)$, the velocity vector with u and w being the components in the x- and z-directions, respectively; ψ is a stream function; $\boldsymbol{u}' = (u', w')$, the vortical velocity vector with u' and w' being the components in the x- and z-directions, respectively. Here, x and z are, respectively, the horizontal and vertical coordinates with z defined positive upwards from the mean surface. In addition, a boundary-layer approximation similar to that used in Longuet-Higgins (1953, 1960) was adopted. When linearized, the resulting governing equations and boundary conditions can be written (Ruvinsky *et al.* 1991) as

$$\nabla^2\phi = 0, \tag{4.1}$$

$$\frac{\partial\phi}{\partial t} + g\eta + 2\nu\frac{\partial^2\phi}{\partial z^2} = 0 \quad \text{on} \quad z = 0, \tag{4.2}$$

$$\frac{\partial\eta}{\partial t} = \frac{\partial\phi}{\partial z} + w' \quad \text{on} \quad z = 0, \tag{4.3}$$

$$\frac{\partial\phi}{\partial z} \to 0 \quad \text{as} \quad z \to -\infty, \tag{4.4}$$

$$\frac{\partial w'}{\partial t} = 2\nu\frac{\partial^3\phi}{\partial x^2\partial z} \quad \text{on} \quad z = 0. \tag{4.5}$$

Here, g is the gravitational acceleration, η is the free surface and ν is the kinematic viscosity. To derive the free-surface boundary condition (4.2), first linearize the viscous normal stress condition to $p/\rho = 2\nu(\partial w/\partial z) \approx 2\nu(\partial^2\phi/\partial z^2)$ on $z = 0$, where $|u'|/|\nabla\phi| = O(k\delta)$ is assumed (Lamb 1932; Ruvinsky *et al.* 1991), with δ being the boundary layer thickness. Then, substitute the linearized Bernoulli equation for the pressure, p, to obtain (4.2). Equation (4.5) is obtained from the linearized boundary layer equation for the rotational velocity components combined with the tangential stress condition on $z = 0$ (Ruvinsky *et al.* 1991; see also Appendix B).

To find the expression for w' in terms of η and ϕ, (4.5) is rewritten, after using the linearized kinematic boundary condition, as

$$\frac{\partial w'}{\partial t} = 2\nu\frac{\partial^3\phi}{\partial x^2\partial z} = 2\nu\frac{\partial^3\eta}{\partial x^2\partial t} \quad \text{on} \quad z = 0. \tag{4.6}$$

Now, integrating (4.6) once in time yields

$$w' = 2\nu\frac{\partial^2\eta}{\partial x^2} + C(x) \quad \text{on} \quad z = 0, \tag{4.7}$$

where, by assuming that the flow is initially inviscid and irrotational, the integration 'constant' $C(x)$ is set to zero. Then, the kinematic free-surface boundary condition is as follows:

$$\frac{\partial\eta}{\partial t} = \frac{\partial\phi}{\partial z} + 2\nu\frac{\partial^2\eta}{\partial x^2} \quad \text{on} \quad z = 0. \tag{4.8}$$

And (4.2) is written as

$$\frac{\partial \phi}{\partial t} = -g\eta + 2\nu\frac{\partial^2 \phi}{\partial x^2} \quad \text{on} \quad z = 0, \tag{4.9}$$

where $-\partial^2\phi/\partial z^2$ is replaced with $\partial^2\phi/\partial x^2$. Equations (4.8) and (4.9) form the closed free-surface boundary conditions modified with the leading-order viscous effects and, in fact, are identical to those obtained by Dias, Dyachenko & Zakharov (2008) using the solutions of the linearized Navier–Stokes equations in the small viscosity limit.

Earlier, Longuet-Higgins (1992) suggested that modified free-surface boundary conditions similar to (4.8) and (4.9) may be used to represent energy dissipation due to wave breaking if the kinematic viscosity, ν, is replaced with the turbulent eddy viscosity, ν_{eddy}. This might be a reasonable eddy viscosity model when short-wavelength scale disturbances, once excited (by wave breaking here), are assumed to be dissipated in the same manner as energy dissipation by kinematic viscosity. Therefore, as a first step towards a more comprehensive parameterization for wave breaking energy dissipation, we simply replace the kinematic viscosity in (4.8) and (4.9) with the eddy viscosity estimated from experimental measurements, as described in the preceding section and we conduct numerical simulations to test the validity of this simple idea.

4.2. *Comparison of numerical solutions with laboratory measurements*

The numerical model is based on an asymptotic expansion in small wave steepness (West *et al.* 1987; Choi 1995) which yields the following nonlinear equations for the surface elevation, $\eta(x, t)$, and the velocity potential at the free surface, $\Phi(x, t)$. When the eddy viscosity terms are included, the model can be written as

$$\frac{\partial \eta}{\partial t} = \sum_{n=1}^{\infty} Q_n[\eta, \Phi] + 2\nu_{eddy}\frac{\partial^2 \eta}{\partial x^2}, \tag{4.10}$$

$$\frac{\partial \Phi}{\partial t} = \sum_{n=1}^{\infty} R_n[\eta, \Phi] + 2\nu_{eddy}\frac{\partial^2 \Phi}{\partial x^2}, \tag{4.11}$$

where Q_n and R_n of $O(ka)^n$ represent the nth-order nonlinear terms that can be found through explicit recursion formulas (for example, Choi, Kent & Schillinger 2005).

In this study, the right-hand sides of the equations are truncated to the third order and the nonlinear evolution equations (4.10) and (4.11) are solved numerically with a pseudo-spectral method based on the fast Fourier transform and a fourth-order Runge–Kutta method to integrate in time. Details of the numerical method can be found in Choi *et al.* (2005). This numerical model has been applied to predict surface wave profiles and local kinetic energy in the breaking criterion study by Tian *et al.* (2008), where excellent agreement with their measurements was shown before wave breaking occurs. In this paper, the applicability of the eddy viscosity model in (4.10) and (4.11) after wave breaking will be explored by comparing numerical solutions with laboratory experiments.

Following Tian *et al.* (2008), initial conditions (i.e. initial surface profile and velocity potential at $z = 0$) are generated with the first wave probe measurements and LWT. Then, numerical simulations are performed in a 48-m-long numerical wave channel, which is discretized with 2^{11} points. A time step of $1/50$ s is employed for the simulations.

During initial numerical tests, we found that the total potential energy (i.e. $\{\eta^2\}$) at the first wave probe did not match the experimental measurements. The discrepancy

was due to viscous effects and nonlinearity (i.e. the initial entire surface elevation as a function of space was generated with the first wave probe measurement and LWT; then it was propagated back to the first probe with the third-order model). Therefore, to match the total potential energy measured at the first wave probe, the linear model without eddy viscosity is solved over the spatial domain from the wavemaker to the location of the first wave probe. The remainder of the tank is assumed to be viscous and the third-order model with the eddy viscosity is solved. A transition layer (~ 1 m) between the linear inviscid and the third-order viscous domain is applied to avoid any transition irregularity of the surface profiles.

In the viscous non-breaking domain, an equivalent kinematic viscosity is applied to the free-surface boundary conditions (see (4.8) and (4.9)) to account for the free-surface damping and the friction and contact-line loss due to the side walls and the tank bottom. For each of the five wave groups, the equivalent kinematic viscosity is estimated with the surface elevation measurements of the non-breaking trains and LWT (i.e. exponential decay prediction; Lamb 1932; Mei 1983; Tulin & Waseda 1999).

During active wave breaking (i.e. for t_{br}), a breaking region based on experimental measurements (i.e. l_{br}) is defined so that the estimated breaking eddy viscosity can be applied to the free-surface boundary conditions. To obtain the eddy viscosity with (3.6) and (3.7), the proportionality coefficients have to be determined. However, our experimental measurements provide no information on the coefficient estimation. To determine the coefficients, θ and θ', one wave group (W1G3, table 1) is used for a trial test. The proportionality coefficients are set to 1; then the trial eddy viscosities estimated with (3.6) and (3.7) are used to run the simulation. Next, numerical results of the total potential energy as a function of space are compared to the experimental measurements. The coefficients are adjusted systematically till good agreement between the numerical and the experimental results are achieved. As mentioned previously, the proportionality coefficients are determined as $\theta = 0.02$ and $\theta' = 0.10$ for wave group W1G3. Finally, these two coefficients are applied to other wave groups to test their applicability. As shown subsequently, good agreement between the numerical and experimental results suggests that the proportionality constants determined from a particular wave group are valid for all our wave groups. We remark that the proportionality constants may need to be adjusted for other experiments with significantly different group structures.

As (3.6) with $\theta = 0.02$ and (3.7) with $\theta' = 0.10$ provide similar estimations of the eddy viscosity (see figure 11) and our tests show that numerical simulations with either eddy viscosity provide virtually the same energy dissipation, we present results of numerical simulations with the eddy viscosity estimated by (3.6). As shown in figure 12, both the magnitude and the trend of the total energy measured in the experiments as a function of space are approximated reasonably well by the numerical results. Most importantly, the numerical results capture the measured energy loss due to wave breaking.

The data oscillations in figure 12 are worth mentioning. As discussed in §3.2.1, these oscillations in the experimental results are partially due to the failure of the linear assumption to estimate the total energy using $\{\eta^2\}$. We numerically examined the total energy, $E(t)$, as a function of time for a non-breaking wave group and found that both the total potential energy, $E_p(t)$, and the total kinetic energy, $E_k(t)$, demonstrate a general decay trend with oscillations present in wave focusing/breaking regions; however, the oscillations of $E_p(t)$ and $E_k(t)$ are 180° out of phase; therefore, the total energy decays monotonically. This finding indicates that the oscillations in the
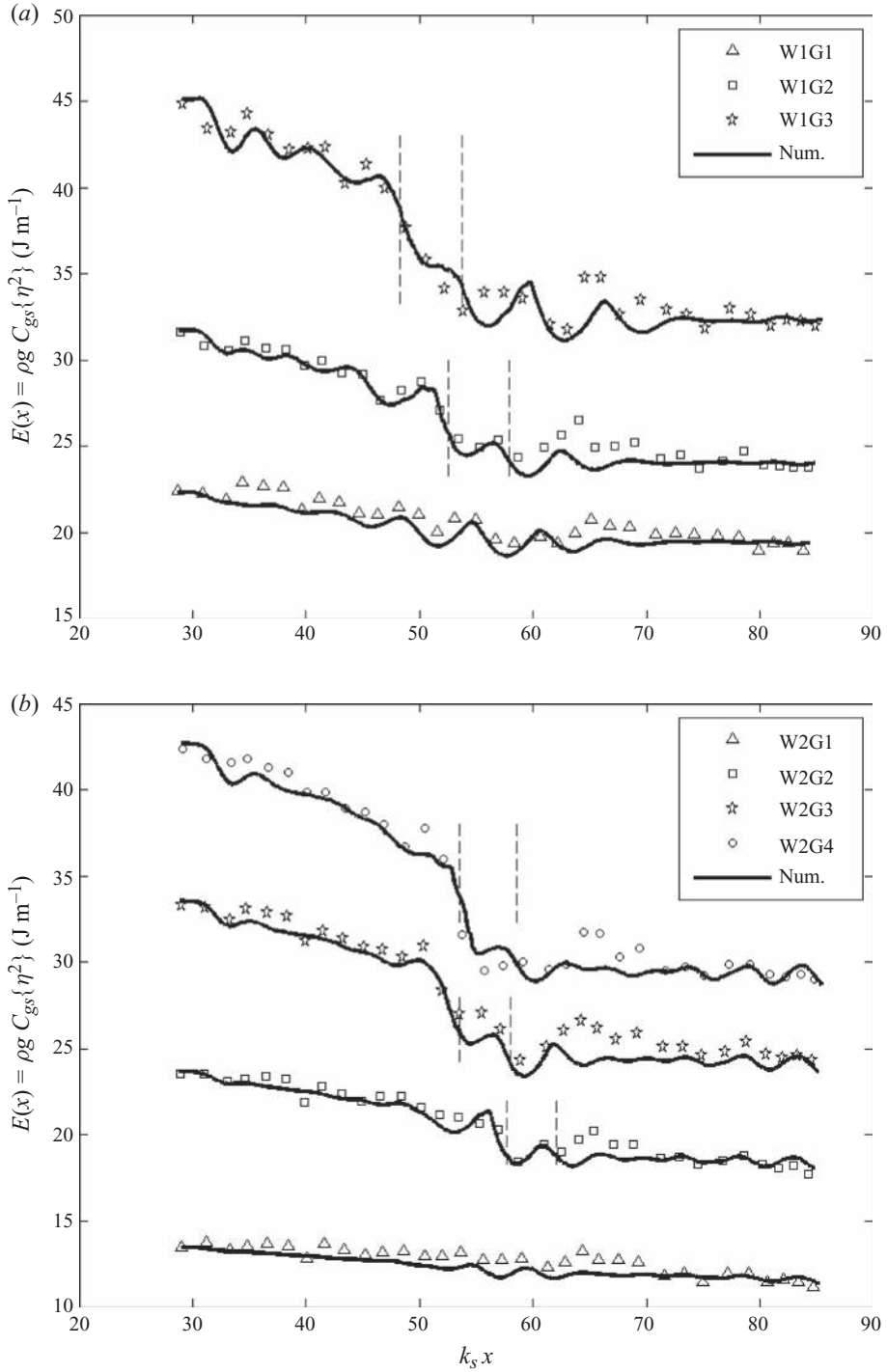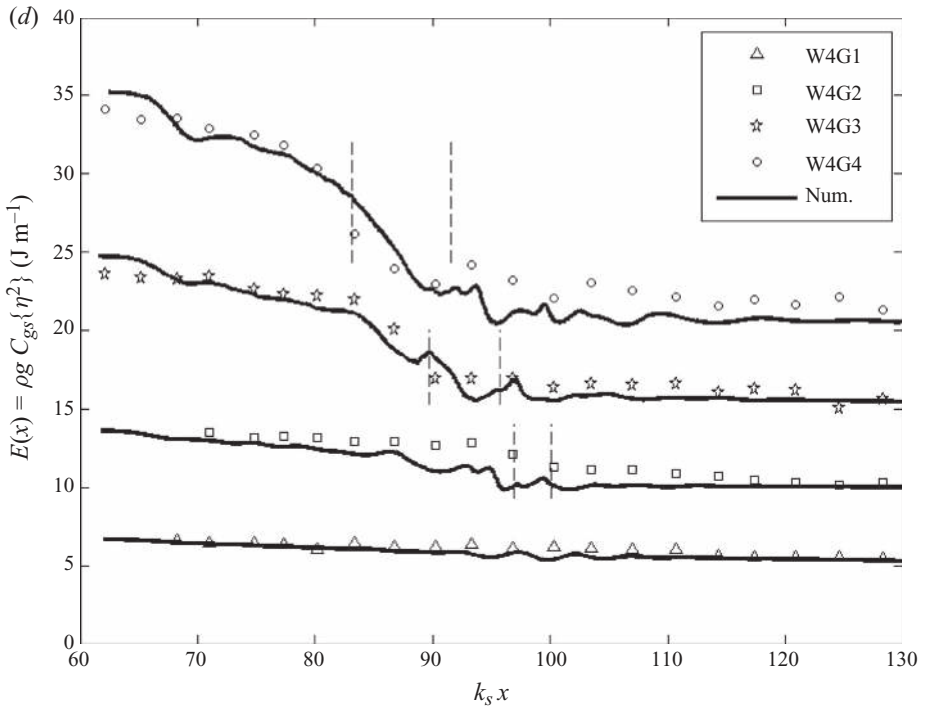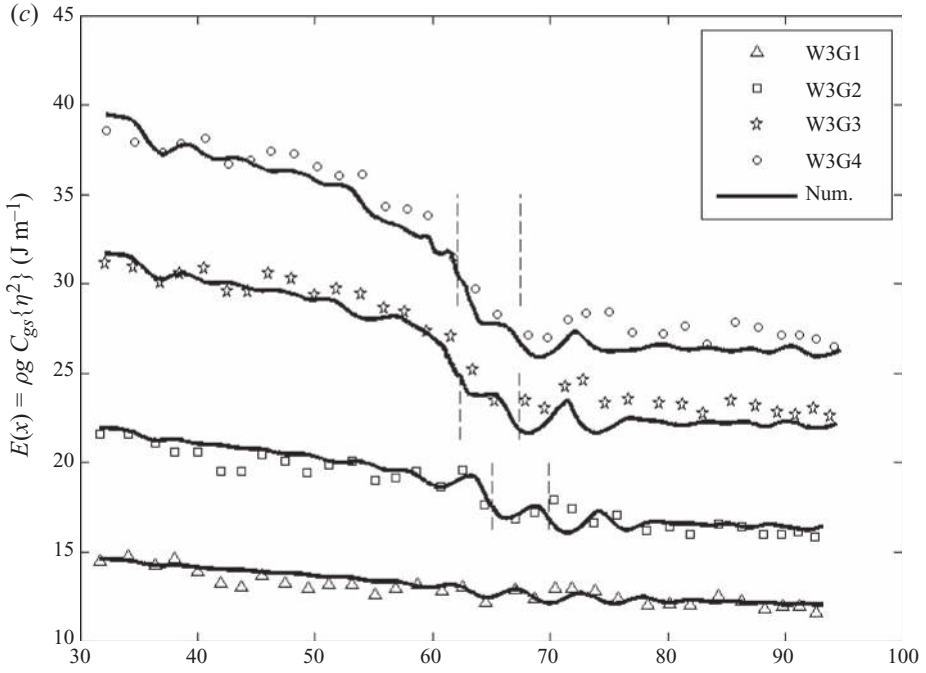
FIGURE 12. For legend see page no. 247

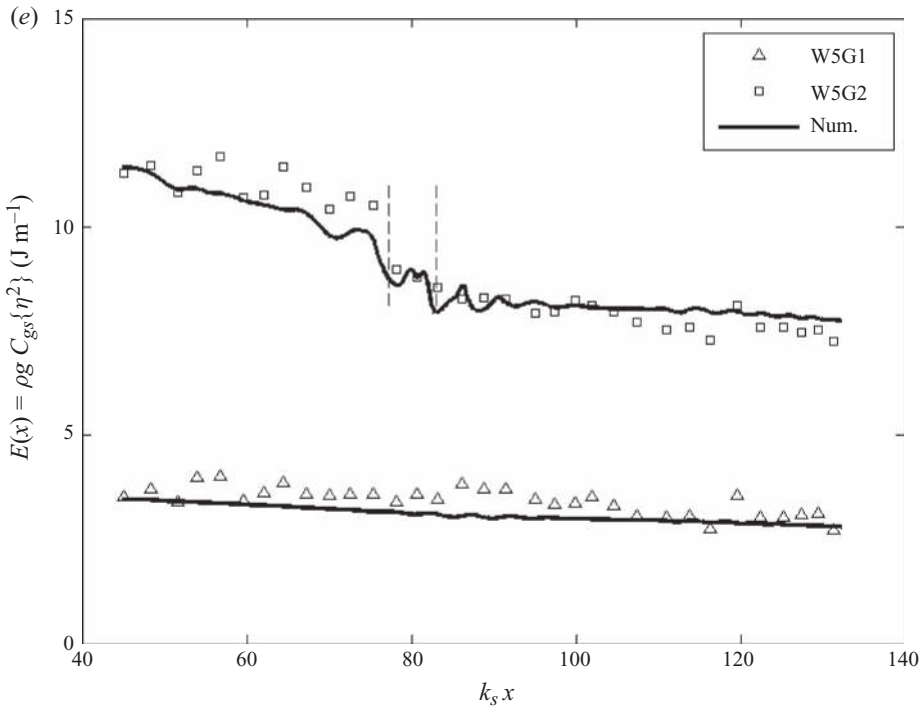FIGURE 12. For legend see page no. 247

FIGURE 12. In graphs (*a*)–(*e*), comparisons of the total energy as a function of space are presented. Symbols represent experimental measurements and solid lines represent numerical results. The vertical dashed lines indicate the wave breaking region.

focusing/breaking regions are mainly due to the failure of the linear assumption in estimating the total energy, as expected.

The surface elevation comparison downstream of wave breaking is also of obvious interest. Figure 13 presents the surface elevation measured at three wave stations along the wave tank: one upstream and two downstream locations relative to wave breaking. For reference, measurements for a non-breaking wave group are also provided. In the figure, dimensional variables are used for a straightforward comparison. Note that our experimental and numerical results show very good agreement not only in the wave amplitude, but also in phase. Some small local discrepancies also appear in the comparisons. For example, the second major peak of the numerical surface elevation at $x = 15.42$ m (W1G3, figure 13*a*) is reduced by a significant amount. Although its cause is not known yet, we believe this is not caused by the eddy viscosity model as a similar reduction is present in the non-breaking wave group, too.

Our numerical study suggests that the simple eddy viscosity model works reasonably well for deep-water breaking waves in terms of energy dissipation. The model is based on simple dimensional analysis, in which a wave breaking time scale, t_{br}, a horizontal wave breaking length scale, l_{br}, and a vertical length scale (breaking wave crest falling height), h, are used. However, to apply this model to numerical simulation, the eddy viscosity has to be determined *a priori* with experimental measurements, and applied in the proper location and during the correct time with both known in advance. These requirements are obviously demanding. Fortunately, our study shows that the local wave steepness S_b and the breaking strength parameter, δ_{br}, proposed by Song & Banner (2002) demonstrate strong correlation with the energy dissipation rate, b_b, and
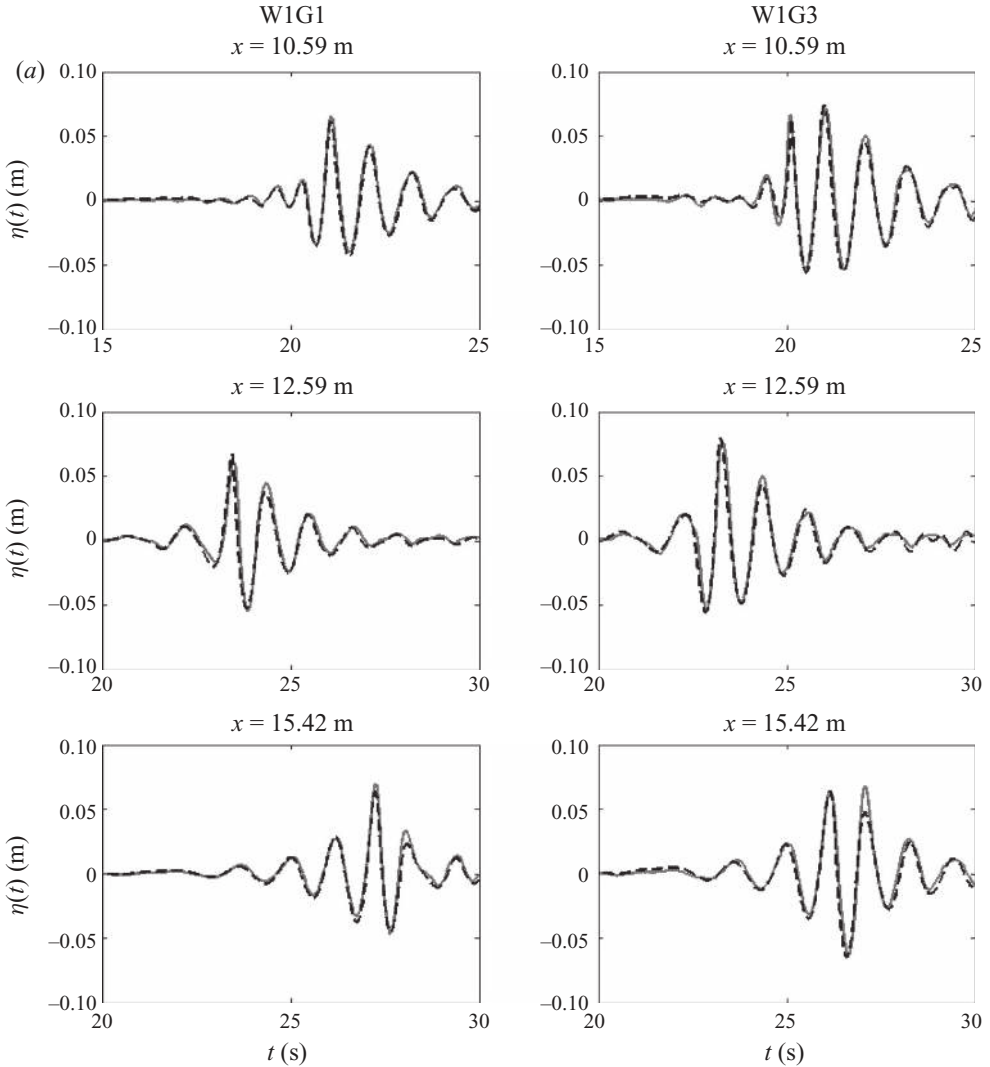
FIGURE 13. For legend see page no. 252

the eddy viscosity, ν_{eddy}. In addition, based on figure 9, t_{br} and l_{br} depend on S_b or δ_{br}; and, for a rough estimation, one may infer the breaking time and the horizontal length based on S_b or δ_{br}. In simulating an individual wave breaking event, for example, the local wave steepness S_b can be computed and monitored throughout the numerical simulation. Once S_b approaches $(S_b)_0$, the eddy viscosity may be implemented (i.e. prior to numerical blow-up).

5. Conclusions

An experimental study of the kinematics and the dynamics of two-dimensional unsteady plunging breakers has been reported. In addition, an eddy viscosity model is proposed to simulate the energy dissipation due to wave breaking and the model is validated with our experimental results.
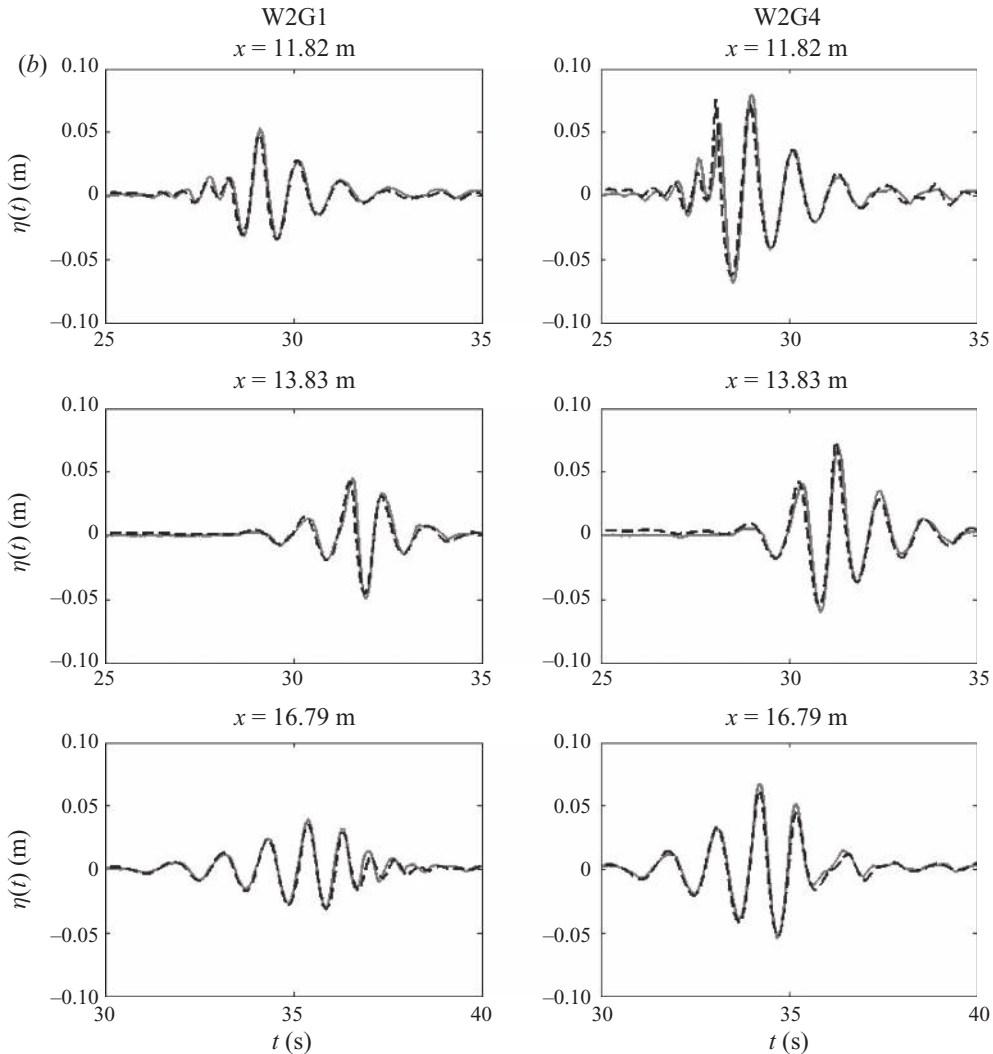
FIGURE 13. For legend see page no. 252

In our experiments, wave surface elevations are measured with both wave probes and high-speed imaging. With the wave probe measurements, wave characteristics associated with the wave group (i.e. S, f_s, k_s, c_s and C_{gs}) are defined and determined. While the centre wave frequency and the associated linear group velocity in a wave group are commonly considered to be the group characteristics, our study illustrates that the spectrally weighted wave frequency (and wavenumber) and group velocity better represent the characteristic properties for wave groups (with constant wave steepness distribution across their amplitude spectra). Based on surface profiles (just prior to wave breaking onset) measured with high-speed imaging, local breaking wavenumber, k_b, local wave steepness, S_b, and breaking wave phase speed, c_b, are determined. We find a strong connection between our wave group characteristics and the local breaking wave parameters (i.e. $S_b/S = 1.237$, $c_b/c_s = 0.9 \pm 0.1$ and $k_b/k_s = 1.25 \pm 0.25$). To our knowledge, these links have not been reported before.
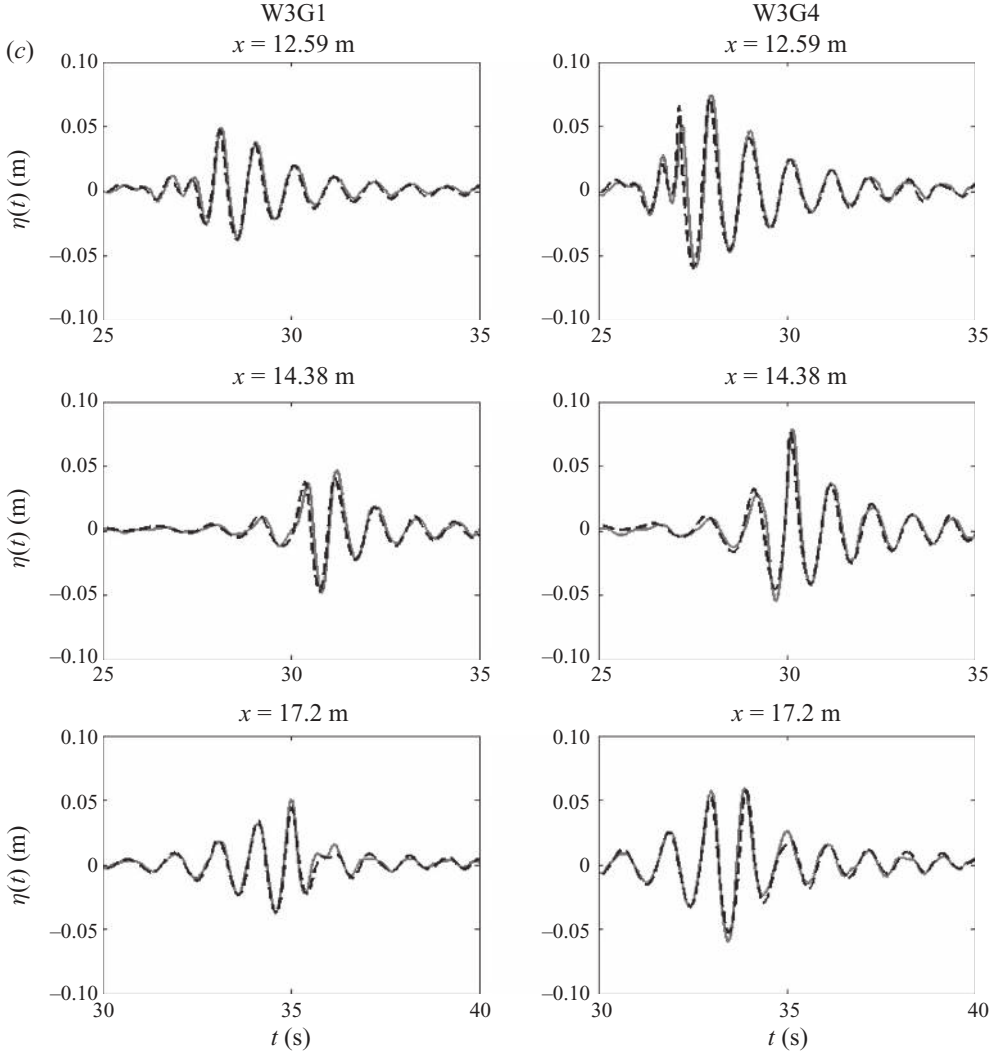
FIGURE 13. For legend see page no. 252

Surface elevation measurements with wave probes are also used to estimate the total energy and the total energy loss. We find that energy loss due to surface damping, contact-line dissipation and friction by the tank sidewalls and the bottom is non-negligible as compared to energy loss due to wave breaking that ranges from 8 % to 25 % of the total pre-breaking energy. More interestingly, both estimated total pre-breaking energy and energy loss due to wave breaking are found to scale accurately with the wave group characteristics (i.e. $E_0 k_s^3/(\rho g)$ versus S and $\Delta E k_s^3/(\rho g)$ versus S). Good correlations are also observed when both the energy and the energy loss are scaled with local wave characteristics (i.e. $E_0 k_b^3/(\rho g)$ versus S_b and $\Delta E k_b^3/(\rho g)$ versus S_b). Based on a linear least-square fit between $\Delta E k_s^3/(\rho g)$ and S, the threshold of S that predicts wave breaking onset is estimated as $S_0 = 0.339$, and hence, $(S_b)_0 = 0.419$ for the same purpose. However, the application of S or S_b as a universal indicator to predict wave breaking and breaking strength needs to be explored further due to the variation of S_0 in different laboratory studies. While the local wave steepness
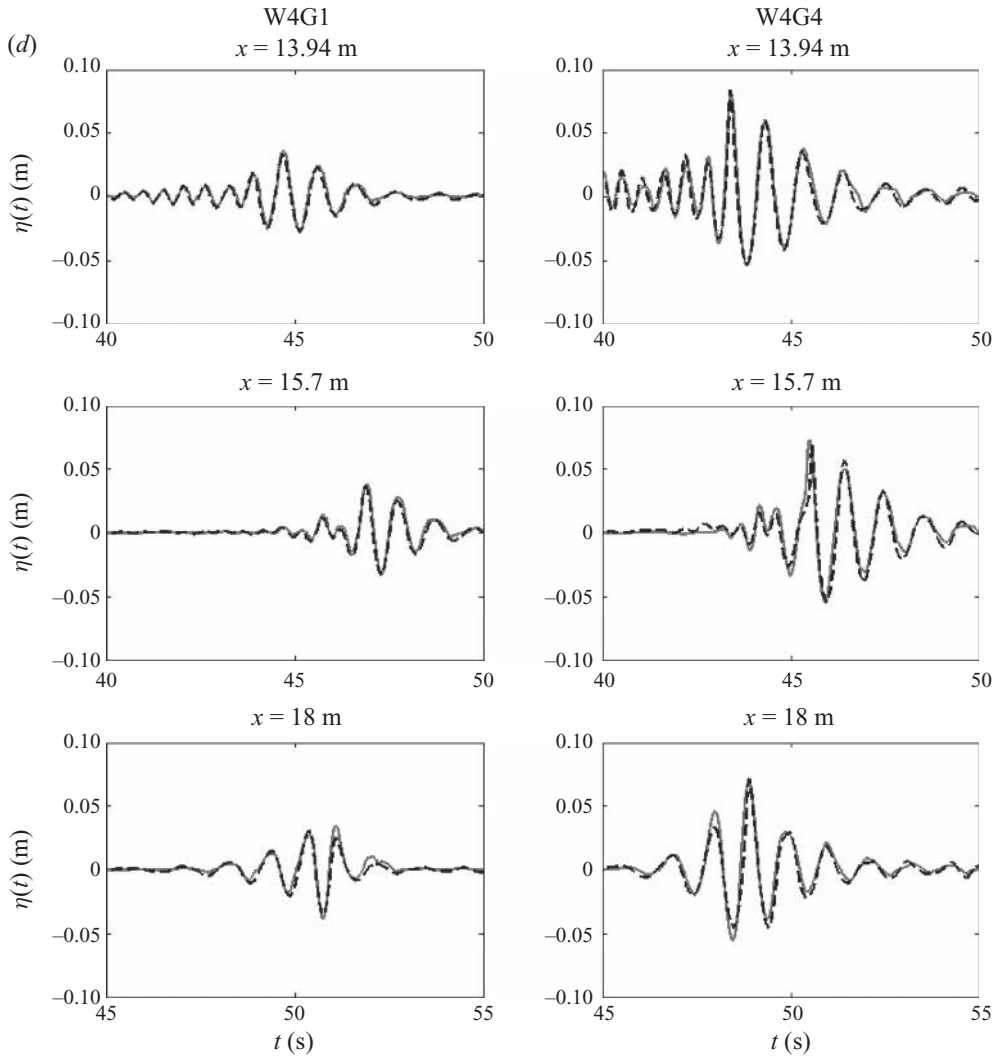
FIGURE 13. For legend see page no. 252

parameter, S_b, seems to be a more universal wave breaking indicator, its performance needs to be further investigated.

Surface profile measurements using high-speed imaging are utilized to determine the breaking criterion parameter, $\delta(t)$, and its magnitude just prior to wave breaking. Our study justifies Song & Banner's (2002) wave breaking criterion which states that $\delta(t)$, with threshold $1.4 \pm 0.1 \times 10^{-3}$, distinguishes wave groups that lead to breaking from those that do not. The breaking parameter immediately before wave breaking (i.e. δ_{br}) increases in general as the energy loss due to wave breaking increases. In addition, δ_{br} can be expressed analytically with the local wave slope S_b; and the relationship is supported by our experimental results.

Breaking time scale and breaking horizontal length scale are defined and obtained with high-speed imaging measurements. The time and length scales depend approximately linearly on S_b, indicating that the breaking process is more violent as S_b increases. The two scales are then used to determine the horizontal breaking wave
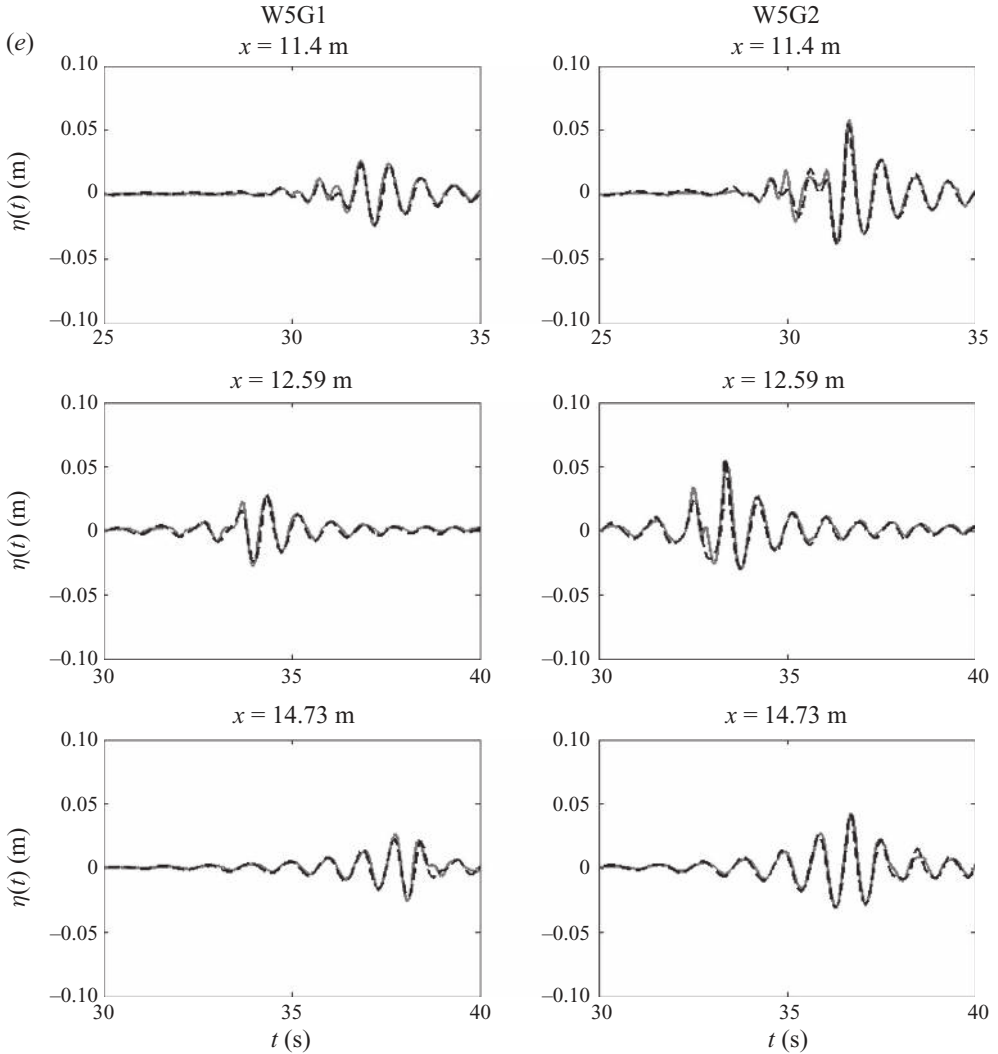
FIGURE 13. (*a*)–(*e*) The comparison of surface elevations measured from three wave stations. Solid line: experimental measurements; dashed line: numerical results. In each of the five sets of graphs, figures in the left column are from the non-breaking wave groups; figures of the most violent breaking wave groups are in the right column. Breaking regions are: [11.28 m, 12.57 m] for W1G3 in (*a*), [12.53 m, 13.71 m] for W2G4 in (*b*), [13.09 m, 14.24 m] for W3G4 in (*c*), [14.11 m, 15.54 m] for W4G4 in (*d*) and [11.72 m, 12.59 m] for W5G2 in (*e*).

crest speed, u_{br}, which is shown to strongly correlate with the breaking wave phase speed, c_b, and the spectrally weighted wave phase speed, c_s.

The energy dissipation rate in the plunging breakers is determined as the ratio of the total energy loss due to wave breaking to the measured breaking time. This estimation method assumes a constant dissipation rate and involves only local wave parameters. The normalized energy dissipation rate (i.e. b_b) is of the order of 10^{-3}, which in general is consistent with previous results, subject to proper data interpretation. Although both S_b and δ_{br} well correlate with b_b, indicating that both parameters can be used to indicate wave breaking strength, S_b appears to have a stronger correlation.

An eddy viscosity model obtained from the viscous free-surface boundary conditions for weakly damped surface waves is adopted and tested numerically with laboratory measurements for energy dissipation due to wave braking. The eddy viscosity is estimated by both dimensional analysis and turbulent energy dissipation rate analysis with measured breaking time and length scales. The two estimations are very close, both of the order of 10^{-3} m^2 s^{-1}. The estimated eddy viscosity also illustrates close correlation with the energy dissipation rate, b_b, and the wave breaking strength parameters, S_b and δ_{br}. The estimated eddy viscosity is employed in simulations that aim to reproduce the experimental tests numerically. Good agreement in energy dissipation obtained from the numerical simulations and the experimental measurements is found and this indicates that the eddy viscosity model could be an effective tool in simulating the energy dissipation in plunging breakers and post-breaking wave profiles.

Appendix A. Nonlinear group velocity

The rate of change of total energy, dE/dt, inside a control volume between two vertical planes bounded by a free surface and a flat bottom is given (Wehausen & Laitone 1960, §8) by

$$\frac{dE}{dt} = F_1 - F_2 \text{ with } F = -\rho \int_{-h}^{\eta} \frac{\partial \phi}{\partial t} \frac{\partial \phi}{\partial x} \, dz, \qquad (A\,1)$$

where F_1 and F_2 represent the energy fluxes per unit length through two vertical planes at x_1 and $x_2 = x_1 + \Delta x$, the left- and right-hand side boundaries, respectively. By substituting into (A.1) Stokes' wave solutions correct to the third order in wave steepenesss (Wehausen & Laitone 1960, §27):

$$\phi = ac_0 \, e^{kz} \sin kx + \cdots,$$

$$\eta = a \left[\cos(kx) + \frac{1}{2} ka \cos(2kx) + \frac{3}{8}(ka)^2 \cos(3kx) + \cdots \right],$$

$$c = c_0 \left[1 + \frac{1}{2}(ka)^2 + \cdots \right],$$

the energy flux averaged over a wavelength $2\pi/k$, $\bar{F}$, can be expanded as

$$\bar{F} = \overline{\rho c \int_{-h}^{\eta} \left(\frac{\partial \phi}{\partial x} \right)^2 dz} = \frac{1}{4} \rho g c_0 a^2 \left(1 + \frac{5}{2} k^2 a^2 + \cdots \right),$$

where $c_0^2 = g/k$ and a is the wave amplitude. The averaged energy flux can also be written as the product of the total energy density and the (nonlinear) group velocity, $\bar{F} = e \, C_g$, where the total energy density averaged over a wavelength is

$$e = \overline{\frac{1}{2} \rho g \eta^2 + \frac{1}{2} \rho \int_{-h}^{\eta} \left[\left(\frac{\partial \phi}{\partial x} \right)^2 + \left(\frac{\partial \phi}{\partial z} \right)^2 \right] dz} = \frac{1}{2} \rho g a^2 \left(1 + \frac{3}{4} k^2 a^2 + \cdots \right).$$

Then, from the two different expressions of $\bar{F}$, the group velocity C_g correct to $O(k^2a^2)$ can be found as

$$C_g = \frac{1}{2}c_0 \left(1 + \frac{7}{4}k^2a^2 + \cdots \right).$$

Notice that, when the effect of nonlinearity is included, this nonlinear group velocity measuring the speed at which energy propagates is different from the classical nonlinear definition of the group velocity (from the kinematic consideration), which can be written as

$$\frac{\partial \omega}{\partial k} = \frac{1}{2}c_0 \left(1 + \frac{5}{2}k^2a^2 + \cdots \right).$$

Appendix B. Derivation of (4.5)

When linearized, the tangential stress condition at $z = 0$ is given by

$$\frac{\partial u}{\partial z} + \frac{\partial w}{\partial x} = 0 \quad \text{on} \quad z = 0. \tag{B 1}$$

After writing $\boldsymbol{u} = \nabla\phi + \boldsymbol{u}'$ and assuming that $|\boldsymbol{u}'|/|\nabla\phi| = O(k\delta)$ (Lamb 1932; Ruvinsky *et al.* 1991) and $|w'|/|u'| = O(k\delta)$ from boundary layer scaling, the leading-order approximation in $k\delta$ of the linearized tangential stress condition yields

$$\frac{\partial u'}{\partial z} = -2\frac{\partial^2 \phi}{\partial x \partial z} \quad \text{on} \quad z = 0. \tag{B 2}$$

On the other hand, the rotational horizontal velocity satisfies the following (linearized) boundary layer equation:

$$\frac{\partial u'}{\partial t} = \nu\frac{\partial^2 u'}{\partial z^2}. \tag{B 3}$$

By differentiating (B.3) with respect to x and using the continuity equation $\partial u'/\partial x + \partial w'/\partial z = 0$, we have

$$\frac{\partial}{\partial z}\left(\frac{\partial w'}{\partial t}\right) = \nu\frac{\partial^3 w'}{\partial z^3}, \tag{B 4}$$

which can be integrated to obtain (4.5):

$$\frac{\partial w'}{\partial t} = \nu\frac{\partial^2 w'}{\partial z^2} = -\nu\frac{\partial^2 u'}{\partial z \partial x} = 2\nu\frac{\partial^3 \phi}{\partial x^2 \partial z} \quad \text{on} \quad z = 0, \tag{B 5}$$

where the continuity equation for $\boldsymbol{u}'$ and the tangential stress condition (B.2) have been used for the last two expressions, respectively.

Appendix C. Integral velocity estimation based on the turbulent energy dissipation analysis by Melville (1994)

Based on the analysis by Melville (1994), the total energy loss rate, ε, in the assumed triangular turbulent region due to wave breaking can be approximated by

$$\varepsilon = \rho u^3 l_{br}/2, \tag{C 1}$$

where l_{br} is the length of turbulent 'whitecap', and is comparable to one characteristic wavelength (see §3.3.1 and figure 9b); therefore, $l_{br} \sim c_b^2/g$. Hence, the dissipation rate
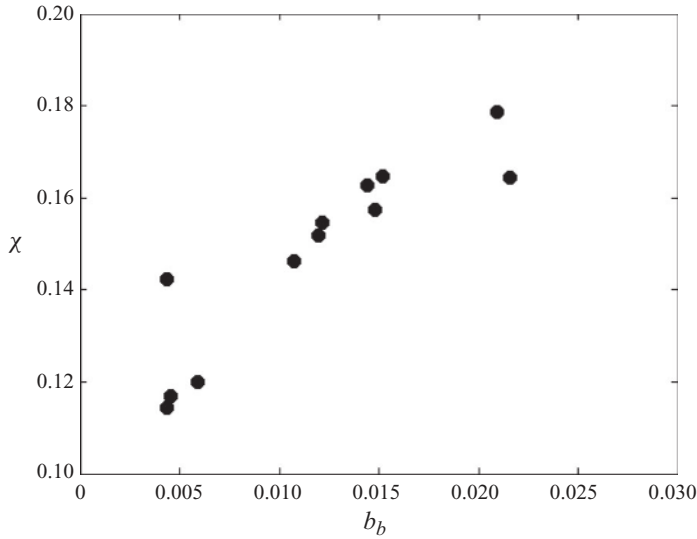
FIGURE 14. Normalized integral speed ($\chi = u/c_b$) as a function of wave breaking strength, b_b. As expected, the integral speed increases as wave breaking intensifies.

can be rewritten as

$$\varepsilon = \rho \left(\chi c_b\right)^3 \left(\gamma c_b^2 / g\right) = \left(\gamma \chi^3\right) \rho c_b^5 / g. \qquad (C\,2)$$

Here γ is a constant and can be deduced from experimental measurements and $u = \chi c_b$ has been used. Recognizing that the term $(\gamma \chi^3)$ represents b_b, we can evaluate the coefficient $\chi = (b_b / \gamma)^{1/3}$. Figure 14 provides the estimation versus wave breaking strength, b_b. As expected, χ increases as wave breaking intensifies and it agrees well with the estimations by Melville (1994). Therefore, eddy viscosity can be roughly estimated as $\nu_{eddy} \sim \chi c_b h$ (see (3.7)).

With the inertial scaling analysis by Drazen *et al.* (2008), who proposed that $b_b = \alpha(k_b h)^{5/2}$, one may write the eddy viscosity as a function of b by substituting $\chi = (b_b / \gamma)^{1/3}$ and $h = (b_b / \alpha)^{2/5} k_b$ into the above equation; further manipulation gives the eddy viscosity as

$$\nu_{eddy} = \beta b_b^{11/15} c_b / k_b, \qquad (C\,3)$$

where β is a proportionality coefficient. With a least-squares analysis, the proportionality constant, β, is determined to be 0.13 for our wave groups. In addition, this power law relationship between ν_{eddy} and b_b can be approximately replaced with a linear one (figure 11*b*).

REFERENCES

BANNER, M. L. & PEIRSON, W. L. 2007 Wave breaking onset and strength for two-dimensional deep-water wave groups. *J. Fluid Mech.* **585**, 93–115.

BANNER, M. L. & PEREGRINE, D. H. 1993 Wave breaking in deep-water. *Annu. Rev. Fluid Mech.* **25**, 373–397.

BANNER, M. L. & TIAN, X. 1998 On the determination of the onset of breaking for modulating surface gravity water waves. *J. Fluid Mech.* **367**, 107–137.

BONMARIN, P. 1989 Geometric properties of deep-water breaking waves. *J. Fluid Mech.* **209**, 405–433.

CHANG, K. A. & LIU, P. L. F. 1998 Velocity, acceleration and vorticity under a breaking wave. *Phys. Fluids* **10**, 327–329.

CHEN, G., KHARIF, C., ZALESKI, S. & LI, J. 1999 Two-dimensional Navier–Stokes simulation of breaking waves. *Phys. Fluids* **11** (1), 121–133.

CHOI, W. 1995 Nonlinear evolution equations for two-dimensional surface waves in a fluid of finite depth. *J. Fluid Mech.* **295**, 381–394.

CHOI, W., KENT, C. P. & SCHILLINGER, C. 2005 Numerical modeling of nonlinear surface waves and its validation. In *Advances in Engineering Mechanics* (ed. A. T. Chwang, M. H. Teng & D. T. Valentine), pp. 94–110, World Scientific.

DIAS, F., DYACHENKO, A. I. & ZAKHAROV, V. E. 2008 Theory of weakly damped free-surface flows: a new formulation based on potential flow solutions. *Phys. Lett.* A **372**, 1297–1302.

DIAS, F. & KHARIF, C. 1999 Nonlinear gravity and capillary-gravity waves. *Annu. Rev. Fluid Mech.* **31**, 301–346.

DOMMERMUTH, D. G., YUE, D. K. P., LIN, W. M., RAPP, R. J., CHAN, E. S. & MELVILLE, W. K. 1988 Deep-water plunging breakers: a comparison between potential theory and experiments. *J. Fluid Mech.* **189**, 432–442.

DRAZEN, D. A., MELVILLE, W. K. & LENAIN, L. 2008 Inertial scaling of dissipation in unsteady breaking waves. *J. Fluid Mech.* **611**, 307–332.

DUNCAN, J. H. 1981 An experimental investigation of breaking waves produced by a towed hydrofoil. *Proc. R. Soc. Lond.* A **377**, 331–348.

DUNCAN, J. H. 1983 The breaking and non-breaking wave resistance of a two-dimensional hydrofoil. *J. Fluid Mech.* **126**, 507–520.

DUNCAN, J. H. 2001 Spilling breakers. *Annu. Rev. Fluid Mech.* **33**, 519–547.

DUNCAN, J. H., QIAO, H. B., PHILOMIN, V. & WENZ, A. 1999 Gentle spilling breakers: crest profile evolution. *J. Fluid Mech.* **379**, 191–222.

GEMMRICH, J. R., BANNER, M. L. & GARRETT, C. 2008 Spectrally resolved energy dissipation rate and momentum flux of breaking waves. *J. Phys. Oceanogr.* **38**, 1296–1312.

GRUE, J., CLAMOND, D., HUSEBY, M. & JENSEN, A. 2003 Kinematics of extreme waves in deep water. *Appl. Ocean Res.* **25**, 355–366.

GRUE, J. & JENSEN, A. 2006 Experimental velocities and accelerations in very steep wave events in deep water. *Eur. J. Mech.* B/*Fluids* **25**, 554–564.

HARA, T. & MEI, C. C. 1991 Frequency downshift in narrow-banded surface waves under the influence of wind. *J. Fluid Mech.* **230**, 429–477.

JIANG, L., PERLIN, M. & SCHULTZ, W. W. 2004 Contact-line dynamics and damping for oscillating free surface flows. *Phys. Fluids* **16** (3), 748–758.

KWAY, J. H. L., LOH, Y. S. & CHAN, E. S. 1998 Laboratory study of deep water breaking waves. *Ocean Engng* **25**, 657–676.

LAKE, B. M., YUEN, H. C., RUNGALDIER, H., & FERGUSON, W. E. 1977 Nonlinear deep-water waves: theory and experiment. Part 2. Evolution of a continuous wave train. *J. Fluid Mech.* **83**, 49–74.

LAMARRE, E. & MELVILLE, W. K. 1991 Air entrainment and dissipation in breaking waves. *Nature* **351**, 469–472.

LAMB, H. 1932 *Hydrodynamics.* 6th edn. Cambridge University Press.

LOEWEN, M. R. & MELVILLE, W. K. 1991 Microwave backscatter and acoustic radiation from breaking waves. *J. Fluid Mech.* **224**, 601–623.

LONGUET-HIGGINS, M. S. 1953 Mass transport in water waves. *Phil. Trans. R. Soc. Lond.* A **245**, 535–581.

LONGUET-HIGGINS, M. S. 1960 Mass transport in the boundary layer at a free oscillating surface. *J. Fluid Mech.* **8**, 293–306.

LONGUET-HIGGINS, M. S. 1992 Theory of weakly damped Stokes waves: a new formulation and its physical interpretation. *J. Fluid Mech.* **235**, 319–324.

LONGUET-HIGGINS, M. S. & COKELET, E. D. 1976 The deformation of steep surface waves on water. I. A numerical method of computation. *Proc. R. Soc. Lond.* A **350**, 1–26.

MEI, C. C. 1983 *The Applied Dynamics of Ocean Surface Waves.* Wiley-Interscience, p. 385.

MELVILLE, W. K. 1982 The instability and breaking of deep-water waves. *J. Fluid Mech.* **115**, 165–185.

MELVILLE, W. K. 1994 Energy-dissipation by breaking waves. *J. Phys. Oceanogr.* **24**, 2041–2049.

MELVILLE, W. K. 1996 The role of surface-wave breaking in air–sea interaction. *Annu. Rev. Fluid Mech.* **28**, 279–321.

MELVILLE, W. K. & MATUSOV, P. 2002 Distribution of breaking waves at the ocean surface. *Nature* **417**, 58–63.

MELVILLE, W. K., VERON, F. & WHITE, C. J. 2002, The velocity field under breaking waves: coherent structures and turbulence. *J. Fluid Mech.* **454**, 203–233.

NEPF, H. M., WU, C. H. & CHAN, E. S. 1998 A comparison of two- and three-dimensional wave breaking. *J. Phys. Oceanogr.* **28**, 1496–1510.

PERLIN, M., HE, J. H. & BERNAL, L. P. 1996 An experimental study of deep water plunging breakers. *Phys. Fluids* **8** (9), 2365–2374.

PERLIN, M., LIN, H. J. & TING, C. L. 1993 On parasitic capillary waves generated by steep gravity waves: an experimental investigation with spatial and temporal measurements. *J. Fluid Mech.* **255**, 597–620.

PERLIN, M. & SCHULTZ, W. W. 2000 Capillary effects on surface waves. *Annu. Rev. Fluid Mech.* **32**, 241–274.

PHILLIPS, O. M. 1977 *The Dynamics of the Upper Ocean.* Cambridge University Press.

PHILLIPS, O. M. 1985 Spectral and statistical properties of the equilibrium range in wind-generated gravity-waves. *J. Fluid Mech.* **156**, 505–531.

PHILLIPS, O. M., POSNER, F. L. & HANSEN, J. P. 2001 High range resolution radar measurements of the speed distribution of breaking events in wind-generated ocean waves: surface impulse and wave energy dissipation rates. *J. Phys. Oceanogr.* **31**, 450–460.

RAPP, R. J. & MELVILLE, W. K. 1990 Laboratory measurements of deep-water breaking waves. *Phil. Trans. R. Soc. Lond.* A **331**, 735–800.

RUVINSKY, K. D., FELDSTEIN, F. I. & FREIDMAN, G. I. 1991 Numerical simulations of the quasi-stationary stage of ripple excitation by steep gravity-capillary waves. *J. Fluid Mech.* **230**, 339–353.

SCHULTZ, W. W., HUH, J. & GRIFFIN, O. M. 1994 Potential energy in steep and breaking waves. *J. Fluid Mech.* **278**, 201–228.

SKYNER, D. 1996 A comparison of numerical predictions and experimental measurements of the internal kinematics of a deep-water plunging wave. *J. Fluid Mech.* **315**, 51–64.

SONG, J. B. & BANNER, M. L. 2002 On determining the onset and strength of breaking for deep water waves. Part I. Unforced irrotational wave groups. *J. Phys. Oceanogr.* **32**, 2541–2558.

STANSELL, P. & MACFARLANE, C. 2002 Experimental investigation of wave breaking criteria based on wave phase speeds. *J. Phys. Oceanogr.* **32**, 1269–1283.

STOKES, G. G. 1880 Supplement to a paper on the theory of oscillatory waves. *Math. Phys. Papers* **1**, 314–326.

SULLIVAN, P. P., MCWILLIAMS, J. C. & MELVILLE, W. K. 2004 The oceanic boundary layer driven by wave breaking with stochastic variability. Part 1. Direct numerical simulations. *J. Fluid Mech.* **507**, 143–174.

THORPE, S. A. 1993 Energy-loss by breaking waves. *J. Phys. Oceanogr.* **23**, 2498–2502.

TIAN, Z. G., PERLIN, M. & CHOI, W. 2008 Evaluation of a deep-water wave breaking criterion. *Phys. Fluids* **20**, 066604.

TRULSEN, K. & DYSTHE, K. 1997 Frequency downshift in three-dimensional wave trains in a deep basin. *J. Fluid Mech.* **352**, 359–373.

TULIN, M. P. & WASEDA, T. 1999 Laboratory observations of wave group evolution, including breaking effects. *J. Fluid Mech.* **378**, 197–232.

WEHAUSEN, J. V. & LAITONE, E. V. 1960 *Surface Waves. Handbook of Physics*, vol. 9. Springer. http://www.coe.berkeley.edu/SurfaceWaves/

WU, C. H. & NEPF, H. M. 2002 Breaking criteria and energy losses for three-dimensional wave breaking. *J. Geophys. Res. Oceans* **107** (C10), 3177.

YAO, A. F. & WU, C. H. 2005 Incipient breaking of unsteady waves on sheared currents. *Phys. Fluids* **17**, 082104.